

Antonija-Ruzica Ferbezar, BSc

Investigation of selected Zr-based metal-organic frameworks as solid-state ion conductors

MASTER'S THESIS

to achieve the university degree of
Master of Science
Master's degree programme: Chemistry

submitted to

Graz University of Technology

Supervisors

Martin Wilkening, Univ.-Prof. Dr.rer.nat.
Institut für Chemische Technologie von Materialien
Ilie Hanzu, Ass.-Prof. Dr.
Institut für Chemische Technologie von Materialien

AFFIDAVIT

I declare that I have authored this thesis independently, that I have not used other than the declared sources/resources, and that I have explicitly indicated all material which has been quoted either literally or by content from the sources used. The text document uploaded to TUGRAZonline is identical to the present master's thesis.

Date, Signature

Abstract

Metal-organic frameworks (MOFs) are porous coordination polymers, which are potentially suitable as solid-state ionic conductors. For the preparation of solid electrolytes, MOFs have many attractive features such as easily synthesized and tailorable structures, functional tunability, and the ability to host various cationic species, including alkali ions. In addition, most MOFs are electronic insulators due to limited charge carrier mobility. In this work, three isostructural zirconium-based metal-organic frameworks, namely UiO-66, UiO-66-NH₂ and UiO-66-(OH)₂ were synthesized and grafted with lithium 3-methyl-3-pentoxide. The pristine and modified MOFs were soaked with an ionic liquid [EMIM][FSI] in order to enable ion transport in the pores and to enhance ionic conductivity. The solid material filled with ionic liquid is called ionogel. In general, UiO-66 exhibits proton conductivity in presence of host molecules such as water or ionic liquids. In this study, not only the proton conductivity of the pristine MOFs, but the potential lithium ion conduction mediated by an ionic liquid in the post-modified MOFs is investigated. The successful synthesis and activation of the MOFs were confirmed by x-ray powder diffraction and BET-measurements. The confinement of [EMIM][FSI] in the pores of the MOFs was verified by ATR-measurements. The proton- and potential lithium-ion conductivity of the ionogels were investigated with impedance spectroscopy.

Kurzfassung

Metallorganische Gerüste (MOFs) sind poröse Koordinationspolymere, die aufgrund vielversprechender Eigenschaften zahlreiche potenzielle Anwendungsgebiete haben. In dieser Forschungsarbeit wird der Fokus auf Anwendung als Festkörperelektrolyten in elektrochemischen Speichersystemen gelegt. Die Struktur und Eigenschaften dieser porösen Materialklasse können durch die Synthese und Post-Modifikationen gezielt eingestellt werden. Als die wichtigsten Merkmale der MOFs zählen die effiziente und schnelle Darstellung, die leichte Porenfunktionalisierbarkeit, eine große aktive Oberfläche und das Einlagerungsvermögen der Fremdmoleküle oder Ionen in den Poren. Die meisten MOFs sind aufgrund der eingeschränkten Mobilität der Ladungsträger elektronische Isolatoren. Zumal sie Fremdmoleküle in die Poren aufnehmen können, kann die Leitfähigkeit durch Einkapselung von Lithium Ionen und ionischer Flüssigkeit in den Poren erhöht werden. Es wurden drei isostrukturelle auf Zirconium basierte MOFs hergestellt und mit Lithium-3-Methyl-3-pentoxid postsynthetisch modifiziert. Anschließend wurden die ursprünglichen- sowie auch die modifizierten MOFs mit ionischer Flüssigkeit [EMIM][FSI] behandelt. Diese Komposite, die auf immobilisierte ionische Flüssigkeiten in den Poren von festen porösen Stoffen beruhen, werden als Ionogele bezeichnet. Die kationen- und protonenleitende Eigenschaften dieser Komposite werden mit Impedanzspektroskopie charakterisiert. Die erfolgreiche Synthese und Aktivierung der MOFs wurde mit Röntgen-Pulverdiffraktometrie und BET-Messungen bestätigt. Die Herstellung der Ionogele beziehungsweise die erfolgreiche Einkapselung der ionischen Flüssigkeit in den Poren wurde mit ATR-FTIR nachgewiesen.

Danksagung

An dieser Stelle möchte ich mich bei denjenigen bedanken, die mich beim Erfassen meiner Masterarbeit unterstützt haben.

Besonderer Dank gilt zunächst meinem Betreuer, Herrn Ass.-Prof. Dr. Ilie Hanzu, der mich richtungsweisend und mit viel Engagement während meiner Arbeit begleitet hat. Des Weiteren möchte ich mich ganz herzlich bei Univ.-Prof. Dr. Martin Wilkening bedanken, der mir die Gelegenheit gegeben hat, in seiner hervorragenden Arbeitsgruppe arbeiten zu können. Ein großer Dank gilt auch für die gesamte Arbeitsgruppe, dessen Mitarbeiter immer hilfsbereit waren. Für die Unterstützung bei der praktischen Arbeit im Labor und Auswertung meiner Ergebnisse möchte ich mich besonders beim Dr. Roman Zettl bedanken.

Nicht zuletzt bedanke ich mich bei meinen Eltern, die mir finanzielle und seelische Unterstützung während meiner gesamten Studienzeit gewährleistet haben.

Contents

1. Introduction	1
2. Theoretical aspects	1
2.1. Lithium-ion batteries	1
2.1.1. Active materials for Li-ion batteries	3
2.2. Solid-state electrolytes	7
2.2.1. Ionogels	9
2.2.2. Metal-organic frameworks	9
2.3. Characterization techniques	11
2.3.1. X-ray powder diffraction (XRD)	11
2.3.2. Impedance spectroscopy	12
3. Experimental	14
3.1. Synthesis of UiO-66, UiO-66-NH ₂ and UiO-66-(OH) ₂	14
3.2. Synthesis of Lithium 3-methyl-3-pentoxide	15
3.3. Grafting	16
3.4. Preparation of ionogels	17
4. Results and discussion	19
4.1. Powder XRD and BET Analysis	19
4.2. ATR-FTIR	24
4.3. Impedance spectroscopy	27
4.3.1. Ionogels based on UiO-66	28
4.3.2. Ionogels based on UiO-66-NH ₂	33
4.3.3. Ionogels based on UiO-66-(OH) ₂	38
5. Conclusion	43
References	44
A. List of abbreviations	49
B. Appendix	50

1. Introduction

The demand for light-weight energy storages for portable electronic devices and especially for electric-powered vehicles (EVs) has been rapidly growing over the past few decades. Li-ion batteries (LIBs) are considered to be the best choice for efficient energy storage. They have attracted great attention due to their high energy density, long cycle life, relatively high power density, low self-discharge rate and absence of memory effects [1] [2]. An ideal battery, however, that meets all performance requirements for the EV market to expand over the internal-combustion-engine vehicles still does not exist. The costs, energy density, and most importantly, operational safety are still limited by the battery chemistry and mechanics [1, 3, 4]. Lack of mechanical, thermal and electrical stability can cause short circuits in the cell, finally leading to thermal runaway. Failure of a single cell will trigger a chain reaction and consequently lead to failure of the whole battery pack [5]. Beside separators, electrolytes are some of the most vulnerable part of battery cells. Liquid, organic electrolytes are extremely flammable and offer no mechanical stability. Further issues with non-aqueous electrolytes are the lack of support for high voltage cathodes and lithium metal anode. Operation at high voltages causes electrolytic decomposition and the lithium metal anode promotes the formation of lithium dendrites. Lithium dendrites may result in breaking through the separator leading to short circuit on contact with the other electrode [6].

Nowadays, many researchers are working on solid-state electrolytes, which are supposed to solve many of the problems mentioned above. Solid electrolytes are both separator and electrolyte in solid-state-batteries (SSBs) and improve safety for large-scale applications such as in electric vehicles. Such batteries also offer high energy density when metal lithium anodes are used, and a wide range of operating temperatures [7]. Despite all the advantages, SSBs are far away from becoming the ideal battery for large-scale applications. The rareness of good ionic conductor materials and the poor interface compatibility between the solid electrolyte and electrodes limit the battery performance in terms of cycle life and capacity [7] [8].

The research is intensively ongoing to find the suitable battery chemistry which provides mechanical, electrochemical, and thermal stability. In this work, a win-win combination of solid and liquid conductors was investigated as a potential solid-state electrolyte. This material consists of a high conductive ionic liquid and a thermal and mechanical stable metal-organic framework. The so-called ionogels may provide good solutions to safety- and capacity challenges [9].

2. Theoretical aspects

2.1. Lithium-ion batteries

Lithium-ion batteries are secondary or rechargeable batteries which contain lithium ions in their primary functional components. Compared to other battery technolo-

gies, LIBs have one of the highest gravimetric- (expressed in Wh kg^{-1}) and volumetric energy densities (expressed in Wh L^{-1})[10]. This is due the facts that lithium is the third lightest element ($M= 6.94 \text{ g mol}^{-1}$, $\rho= 0.53 \text{ g cm}^{-3}$) with a small ionic ratio, and has the lowest electrochemical potential (-3.04 V vs. standard hydrogen electrode).

Batteries are built up of electrochemical cells that are connected in series and parallel patterns. Each electrochemical cell consists of a cathode, an anode, a non-aqueous electrolyte and a separator. In Li-ion electrochemical cells, the anode and cathode store lithium and are separated by an electrolyte which contains lithium ions. The separator acts as a physical barrier between the two electrodes, but allows the exchange of the lithium ions through the electrolyte it contains. The basic working principle of a Li-ion cell is illustrated in Figure 1 and 2. During the discharging process, the potential difference between the electrodes forces the lithium ions to leave the anode and intercalate into the cathode. Simultaneously, the electrons which are released in the redox reaction flow from the anode into the cathode through the external circuit. This provides electrical energy to the connected electrical load.

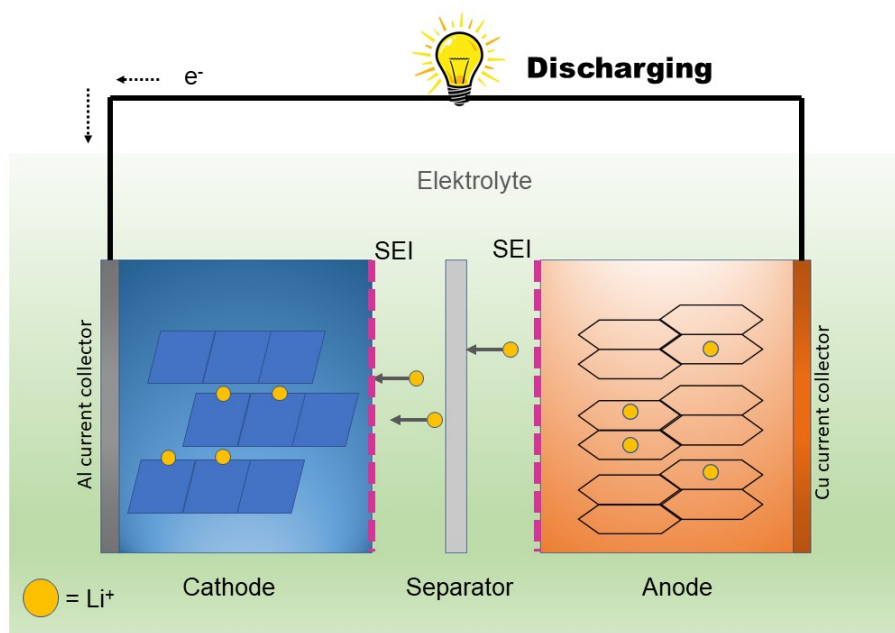


Figure 1: Illustration of the discharging process taking place in a Li-ion galvanic cell.

The opposite happens during the charging process. The anode and cathode are connected to an external electrical supply. Lithium ions leave the cathode and move to the anode through the electrolyte while the electrons move to the same direction externally. In this way, the external energy is stored in the electrode in form of chemical energy.

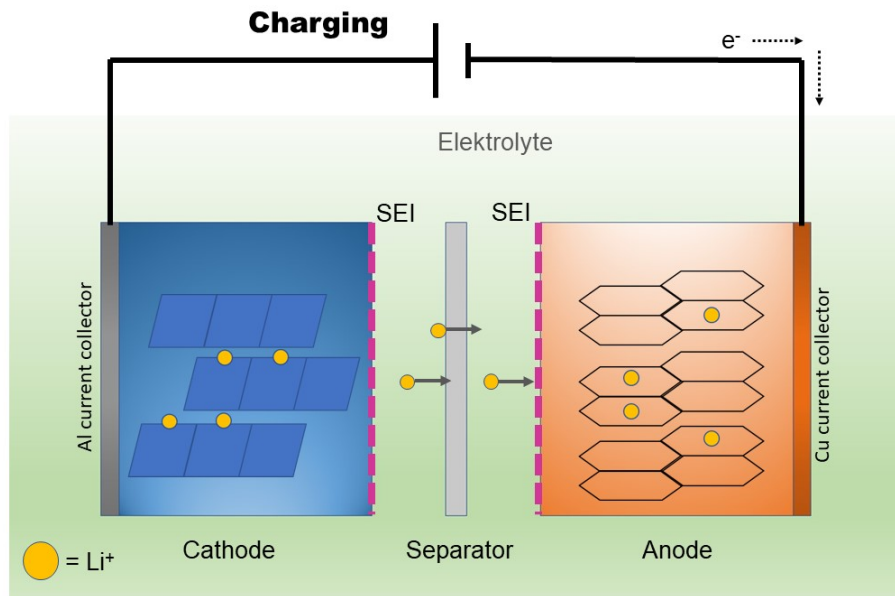


Figure 2: Illustration of the charging process taking place in a Li-ion rechargeable cell.

The active electrode- and electrolyte materials are critical to the battery performances [11]. For example, the storage capacity and cell potential which determine the energy density, are dependent directly on the intrinsic properties of the electrode materials. Other performance parameters like cyclability are affected by the solid electrolyte interphase (SEI). The SEI is a passive layer that has the important role of kinetically stabilizing the electrodes operating outside the thermodynamic potential window of the electrolyte. The abundance, environmental impact, and cost of the materials are considered as well in selecting the right battery chemistry for automotive applications.

2.1.1. Active materials for Li-ion batteries

The pace of improvement in battery technology is very slow and today's technology is still limited. To meet the automotive requirements with a focus on high voltage- and high capacity systems, Li-ion batteries need to be improved by the development of cathode, anode, binders, separators, electrolytes, current collectors, and packaging materials. The ideal electrode materials must have high lithium storage capacity and enable reversible redox reactions. The anode and cathode should have a low and high redox potential, respectively. The ideal electrolyte must support the working voltage of the electrodes with a wide electrochemical stability window (ESW). Further important requirements are thermal stability, high ionic conductivity and low cost. Solid-state electrolytes provide additional mechanical stability and are considered as leading electrolytes in terms of operational safety. They will

be discussed in the next section.

Commercial anodes are dominated by carbonaceous materials [12, 13] which include natural and synthetic graphite, activated carbon, carbon black, and graphene. The most common are graphite based. Graphite is abundant, cheap, and has a high electronic conductivity. The lithium ions intercalate into the graphite and generate LiC_6 which corresponds to a specific capacity of 372 mA h g^{-1} . Since the anode is one of the limiting factors in terms of capacity, the development of new anode materials is crucial. Silicon anodes are of great interests since they have a theoretical capacity of more than 10 times that of graphite. On the other hand, there are few severe disadvantages such as poor electronic conductivity and volume change. During the intercalation of Li, the material can expand up to 400 %, which leads to malfunction of the battery cell [12]. With respect to the energy density, the Li metal anode is considered to be the ideal anode material. The theoretical capacity of 3860 mA h g^{-1} and the very low working potential make the Li metal anode as a promising candidate for high-energy density batteries [14]. This type of anode was, in fact, already commercialized, but failed due to severe safety issues. In combination with liquid organic electrolytes, the highly reactive lithium forms a SEI with the electrolyte; however, an uncontrolled formation of lithium dendrites occurs. This results not only in a short battery lifetime, but leads to a short circuit and severe safety issues. Solid-state electrolytes are expected to tolerate the Li metal anode better and are considered as a solution to suppress the formation of lithium dendrites and enhance the safety.

The next limiting factor in today's battery performance is the cathode. Typical cathode materials for LIBs are made of spinel LMO, olivine LFP, or layered NCM. LMO (Lithium manganese oxide, LiMn_2O_4) provides a high energy density and is a low cost material. However, during discharging, especially under high current, the material experiences phase transitions due to the accumulation of lithium ions on the surface of the LMO. Consequently, the cathode volume changes and a part of the active material becomes damaged, which lowers the capacity. An additional problem is the dissolution of manganese ions in the electrolyte and formation of insoluble LiF on the electrode surface [15, 13]. The olivine LFP (Lithium iron phosphate, LiFePO_4) cathode is known as a safe, eco-friendly and cheap electrode with very good cycling- and thermal stability. They provide, however, low energy density because of the low operating voltage (3.5 - 3.6 V vs. Li^+/Li) compared to other cathodes (operating voltage above 4 V), and poor electronic conductivity [16].

NMC (Lithium Nickel Manganese Cobalt Oxide) is one of the most promising cathode materials and is preferred for automotive batteries.

The NMC-based cathodes were commercialized in several versions which differ in content. The general formula is $\text{LiNi}_x\text{Mn}_y\text{Co}_z\text{O}_2$ ($x+y+z=1$), where x , y , and z represent the contents of nickel, manganese, and cobalt [17].

Variations of the contents dramatically affect the performance of the battery cell [18, 12]. New generation cathodes are composed of high capacity Ni-rich or Li-rich NMC compounds and thus, have a lower content of Co, which is a toxic element

and a critical raw material in short supply. Also, the thermal stability of cobalt layered compounds is far from being perfect [19, 20].

The popular NMC 532 cathode has been used by many electric vehicle manufacturers. The latest generations are NMC 622 and NMC 811 with a significantly higher energy density and lower price than the previous generations. Nickel is the main active redox species in the structure and responsible for high specific energy, but unfortunately suffers from poor thermal stability as well. Manganese maintains a long cycle life and safety. Nevertheless, it is not electrochemically active, thus it decreases the capacity. A higher cobalt content provides thermal stability, increased power capacity [18], electronic conductivity and thus, an excellent rate capability. On the other hand, cobalt is seen as one of the most critical ingredients due to its high cost and problematic supply.

The electrolyte for the current and previous generations of LIBs are lithium salts and additives in organic solvents. Lu et al. [12] summarized the common lithium salts and solvents, which are listed in the following table.

Table 1: Simplified list of common lithium salts of electrolyte in LIBs [12]. The salts were dissolved in EC/DMC (1 M) and the conductivity of was measured at 20 °C. Exceptions are measurements of LiAsF₆ and LiN(SO₂F)₂ at 25 °C.

Salt	Ionic conductivity [mS cm ⁻¹]
LiPF ₆	10.0
LiClO ₄	9.0
LiBF ₄	4.5
LiAsF ₆	11.1
LiN(SO ₂ F) ₂	10.4
LiN(SO ₂ CF ₃) ₂	6.2

Table 2: Simplified list of common organic solvents of electrolyte in LIBs [12].

Solvent	Melting point [°C]	Boiling point [°C]
EC	36.4	248
PC	-48.8	242
DMC	4.6	91
DEC	-74.3	126
EMC	-53	110
DME	-58	84

The ideal solvent should have a high dielectric constant, low viscosity and thermal stability. The most common electrolyte in commercial LIBs consists of LiPF₆ dissolved in carbonate esters. It comes with a small portion of additives (<5% wt%) which stabilize the salt, builds a better SEI on the electrodes, and improve the performance of the electrolyte [21]. This electrolyte exhibits high ionic conductivity, and a relatively fine thermal stability. Yet, it does not meet the requirements

of the future high-energy density lithium-ion battery. The flammability of the organic solvent and the limited ESW cause problems in terms of safety and high voltage performance, respectively.

2.2. Solid-state electrolytes

Solid-state electrolytes (SEs) or ionic superconductors are materials which conduct electricity by transport of ions through the crystalline or amorphous solid structure.

The main characteristics of ionic superconductors are very high ionic conductivity at room temperature ($>10^{-4}$ S cm $^{-1}$) and electronic conductivity that is negligible in comparison to the ionic conductivity. Further characteristics of solid electrolytes are low activation energy (< 1 eV) for fast migration of charge carriers, mechanical integrity and facile conduction pathways. These properties provide a close performance level as the non-aqueous liquid electrolytes in current LIBs. Since liquid organic electrolytes do not satisfy the operational safety standards and high-voltage applications, the SEs are intensively investigated as the main candidate for the "superbattery". They provide high mechanical, electrochemical and thermal stability in the operating temperature range of the battery. In contrast to liquid organic electrolytes, SEs tolerate operation under high voltage. Ultimately, SEs for all-solid-state batteries (Figure 3) should possess the properties of chemical compatibility with the electrodes [22, 23], as well as relatively simple large-scale fabrication with low cost. After many attempts in designing an appropriate solid-state battery, the deficient electrode/electrolyte interfacial compatibility still remains a key fundamental problem and a practical challenge.

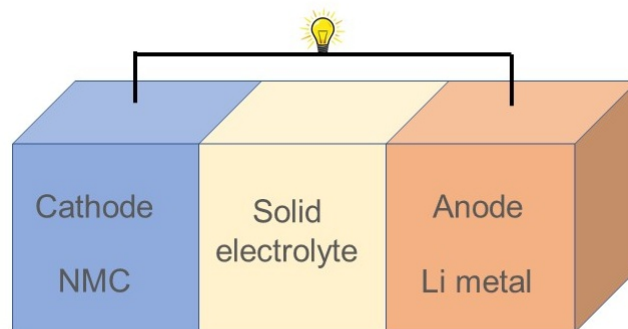


Figure 3: Schematic illustration of an all-solid-state battery

SEs can be roughly divided into inorganic conductors (ISEs), polymer electrolytes (SPEs) and organic-inorganic hybrid composites (CSEs) [7]. Inorganic electrolytes have been widely investigated for their good Li-ion conductivity [24]. The most notable ISEs and their conductivities are listed in the following table:

Table 3: List of various types of ISEs

SE type	SE composition
LISICON	$\text{Li}_{14}\text{ZnGe}_4\text{O}_{16}$
thio-LISICON	$\text{Li}_{10}\text{GeP}_2\text{S}_{12}$
NASICON	$\text{Li}_{1.5}\text{Al}_{0.5}\text{Ge}_{1.5}(\text{PO}_4)_3$ $\text{Li}_{1.5}\text{Al}_{0.5}\text{Ti}_{1.5}(\text{PO}_4)_3$ $\text{LiZr}_2(\text{PO}_4)_3$
LIPON sulfide	$\text{Li}_6\text{P}_3\text{O}_9\text{N}$ $\text{Li}_7\text{P}_3\text{S}_{11}$ $\text{Li}_{10}\text{GeP}_2\text{S}_{12}$ $\text{Li}_6\text{PS}_5\text{X}$ (X= Cl, Br, I)
sulfide based glass	$\text{Li}_2\text{S-SiS}_2$
perovskite	$\text{Li}_{0.33}\text{La}_{0.56}\text{TiO}_3$
garnet	$\text{Li}_7\text{La}_3\text{Zr}_2\text{O}_{12}$ $\text{Li}_{6.4}\text{Fe}_{0.2}\text{La}_3\text{Zr}_2\text{O}_{12}$

Many examples of ISEs including NASICON, perovskite, garnet, and sulfide-type electrolytes show ionic conductivity in the range of 10^{-4} to 10^{-2} S cm^{-1} at room temperature [24, 25]. Since the volume of the electrode active material changes during charging and discharging, SEs should have a moderate elastic modulus and be flexible in respect to the electrodes. Despite the excellent conductivity of some ISEs, the mechanical properties such as rigidity and brittleness cause poor interfacial contact which leads to high contact resistance and favours Li dendrite formation. The behaviour of functional interfaces is crucial in the performance and safety of all-solid-state batteries. The interface should be electrochemically stable at both anodic and cathodic limits. If the interface is not stable, the formation of passive layers is unavoidable [4]. Most ISEs are thermodynamically unstable with respect to electrodes, and the interface would require some kinetic stabilization; the formation of thin, self-limiting passive films is required.

SPEs have received much attention as potential solid electrolytes due to their flexibility, processability, and compatibility with electrodes. In other words, they provide almost everything that ISEs are unable to offer. Unfortunately, the ionic conductivity of most SPEs lies in the range of 10^{-8} to 10^{-5} S cm^{-1} at room temperature, which is not sufficient for applications in high-energy density batteries. SPEs can be classified as conventional polymer-salt complex or dry SPE, plasticized polymer-salt complex, polymer gel electrolyte, rubbery electrolyte and composite polymer electrolyte [23]. Organic-inorganic CSEs are a combination of polymers and inorganic ceramics that offers best properties of both components. CSEs can be composed of a polymer matrix and inert inorganic ceramic fillers or ceramic (active) fast ionic conductors [25]. If inert ceramic fillers are added to the polymer, the crystallization is inhibited and the segmental motions of the polymer chains are allowed. Accordingly, the enabling of the segmental motions of polymers has a great impact on the dynamics of the charge carriers and thus the conductivity [26, 27]. When used as fillers, ceramic fast ionic conductors have a direct impact on the

conductivity, since they offer additional charge transport paths. CSEs are promising materials for solid electrolytes, but still face challenges such as the structural incompatibility and adherence of the polymer matrix to the inorganic component [28].

2.2.1. Ionogels

A successful compromise between liquid and solid electrolytes is offered by the quasi-solid electrolytes, namely ionogel electrolytes. Ionogels are a new class of hybrid materials, consisting of ionic liquid (IL) immobilized in a solid structure. Ionic liquids are salts whose melting points are below 100 °C. They typically consist of large organic cations and smaller inorganic or organic anions. The composition can vary and consequently their properties like polarity, density, viscosity and thermal stability change. Ionic liquids are non-flammable, thermally stable, they show high ion conductivity and have a wide electrochemical potential window [9]. Nevertheless, if simply ionic liquids are used as electrolytes, similar risks as with liquid electrolytes like leakage cannot be avoided.

Depending on the solid component, ionogel electrolytes can be divided into polymeric materials and inorganic materials, such as non-metal oxides [29], metal oxides [30], [31, 32], ionic liquid-tethered nanoparticles [31] and metal-organic frameworks [9, 33]. A critical overview of organic polymer matrices for battery applications is given by Osada *et. al* [34]. In this study, the focus is on metal-organic frameworks, as porous non-conductive solid-state matrix.

2.2.2. Metal-organic frameworks

Metal-organic frameworks (MOFs) are a class of synthetic porous materials and have been studied intensively in the past decade due to their facile preparation, unique properties and wide range of possible applications. They consist of metal ions or clusters which are coupled by multi-dentate organic linkers. The inorganic and organic building blocks, arranged in this way, form a three-dimensional network with a high degree of long-range order (see Figure 4).

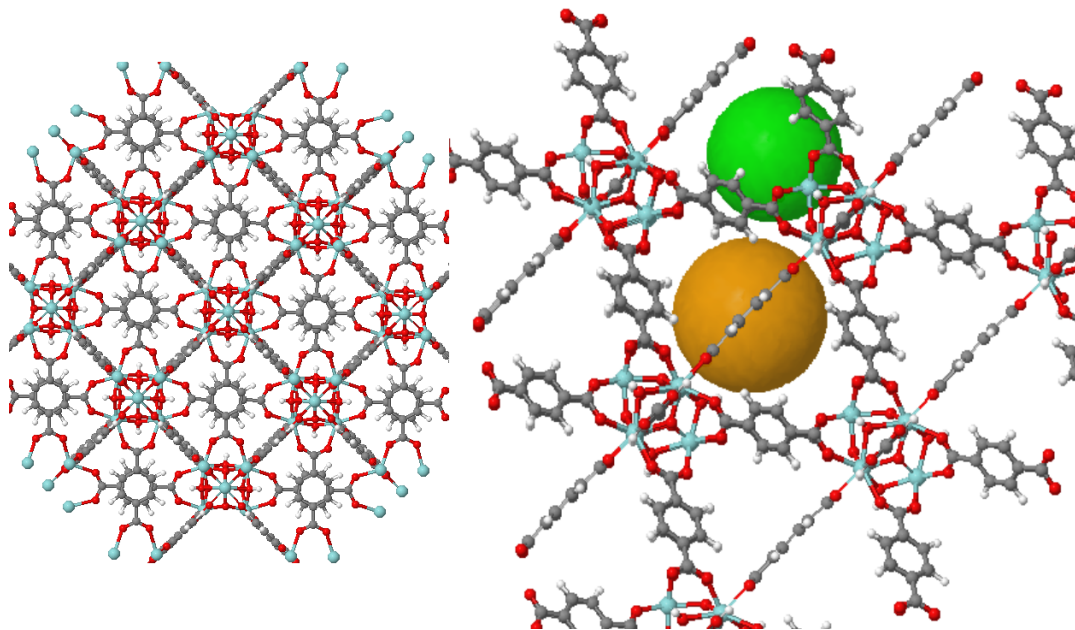


Figure 4: UiO-66 as an example of a metal-organic framework is shown on the left. On the right there are two spheres visible. The big yellow sphere represents the octahedral- and the green sphere represents the tetrahedral cavity in the structure of UiO-66.

The structure, geometry and properties of MOFs can vary depending on the preparation method. A special property of MOFs are the tunable pores, which can vary in size and functionality by modifying the organic linkers, and an extraordinary high specific surface area [35]. Therefore, MOFs are able to host small molecules in the pores and are very well suited for storing and transportation of gases, separation of gases, catalysis, drug delivery etc. [35] [36] [37]. Since the pores are capable for encapsulating ILs, MOFs have been studied intensively for applications as solid electrolytes in batteries.

UiO-66 (Universitetet i Oslo) is built of 12-coordinate cationic $Zr_6O_4(OH)_4^{12+}$ clusters and terephthalate ligands (Benzene-dicarboxylic units or BDC). The structure of the building unit is shown in Figure 5.

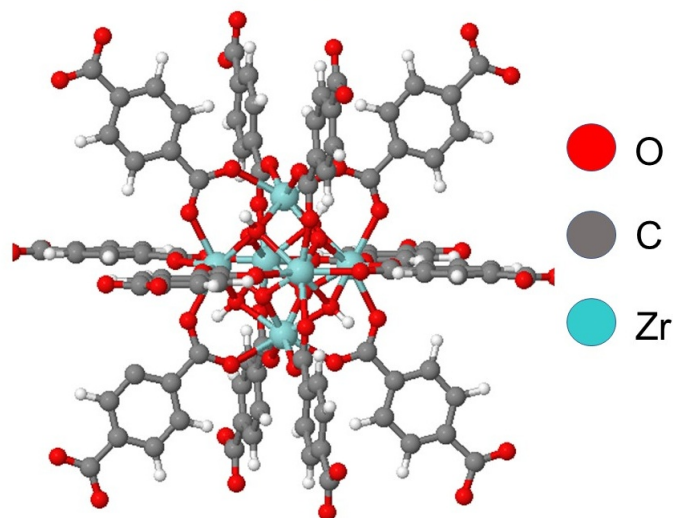


Figure 5: The fundamental building unit of the UiO-66 is presented as a six-centre octahedral zirconium cluster, in which eight-coordinate zirconium cations are connected via BDC linkers.

It shows remarkable features [35, 38, 39] in terms of thermal, chemical stability [40] and porosity, even with functional groups present at the linker units. UiO-66 undergoes decomposition between 350 and 500 °C. Functional groups on linkers can affect the decomposition temperature of the MOFs, thus the UiO-66 derivatives like UiO-66-NH₂ show lower decomposition temperature [41].

UiO-66 and its derivatives show a very low ionic conductivity and are good insulators. When water molecules are encapsulated in the pores, these MOFs show high proton conductivity ($2.3 \times 10^{-3} \text{ S cm}^{-1}$ at 90 °C), and an activation energy of 0.17 eV is estimated and indicates efficient H₂O-mediated transport of protons [42]. The proton conductivity increases from UiO-66 to UiO-66-NH₂ and UiO-66-(OH)₂ since the derivatives with functionalized linkers can donate more protons.

2.3. Characterization techniques

2.3.1. X-ray powder diffraction (XRD)

X-ray powder diffraction (XRD) is a rapid and powerful analytical tool for the characterization of solid materials. The primary purpose of XRD is the identification of crystalline phases. Additionally it provides lattice parameters and information about micro-structure. X-Rays are generated by a cathode ray tube and filtered to obtain a monochromatic radiation. When the collimated and directed beam reaches the crystalline sample, it interacts with the electrons of the atoms in the crystal. Hence, the electrons oscillate and become secondary sources of X-radiation. The coherently scattered X-rays are those that are important for XRD analysis.

The scattered X-radiation can undergo constructive or destructive interference.

The XRD pattern is based on constructive interference of X-rays on a crystalline sample. Constructive interference at specific angles occurs when monochromatic X-rays are scattered by a periodic array with long-range order, or more precisely, when Bragg's law is satisfied,

$$n\lambda = 2d\sin\theta$$

where d is the distance between atomic layers in a crystal, λ is the wavelength of the incident X-ray beam and n is an integer. Powder diffraction stands in contrast to

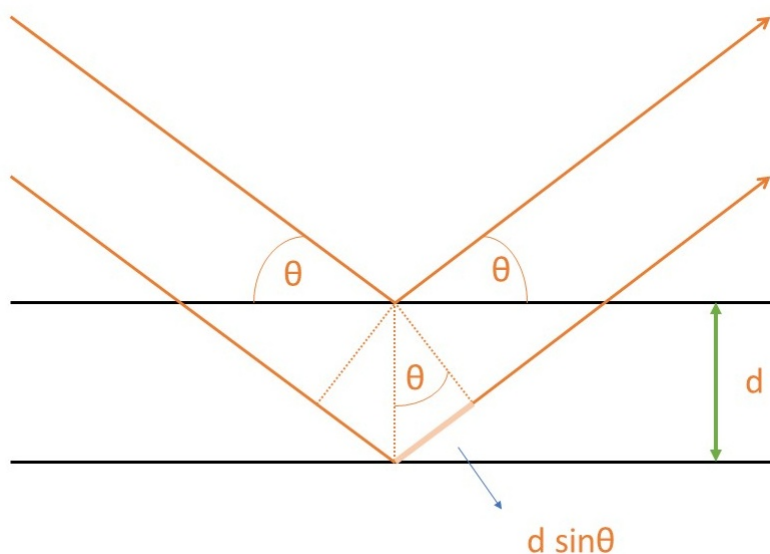


Figure 6: Schematic illustration of Bragg's law.

single crystal diffraction techniques. Instead of one preferred orientation, in powdered samples crystallites are randomly arranged, thus every possible crystalline orientation is statistically equally represented. Each plane of the crystal structure, when in the proper orientation, diffracts X-rays. By rotation of the sample, all possible diffraction orientations of the crystal lattice should be achieved due to the random orientation of the crystallites in powdered material [43, 44].

2.3.2. Impedance spectroscopy

Electrochemical impedance spectroscopy (EIS) is a sensitive and non-destructive technique for characterization of electrochemical systems. EIS measures resistance and capacitance properties of a sample by applying a small sinusoidal excitation AC signal (2-10 mV) over a wide frequency range (from mHz to GHz). The electrochemical cell responds to the excitation signal with an AC current, which is measured and processed using Fourier analysis. When a sinusoidal excitation signal E_t , in form of

$$E_t = E_0 \sin(\omega t)$$

is applied to an electrochemical cell (ω =radial frequency, E_0 =amplitude of the signal), the current response I_t will be a sinusoidal function of the same frequency but shifted in phase ϕ

$$I_t = I_0 \sin(\omega t + \phi)$$

and different in amplitude [45, 46, 47, 48]. Impedance is represented as a complex function.

$$Z(\omega) = Z_0(\cos\phi + i\sin\phi)$$

In contrast to resistance in DC circuits, impedance in AC includes effects of capacitance and inductance, which is summarized as reactance and forms the imaginary part of complex impedance. This phenomenon is responsible for the phase shift between applied voltage and current.

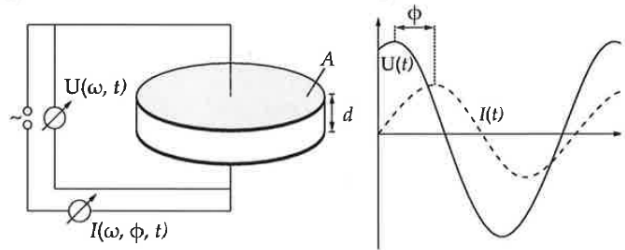


Figure 7: Schematic of a basic impedance spectroscopy setup (left) and phase shift between voltage and current (right).

The real part describes the resistance, which is in-phase with the applied voltage. The easiest way to assess the stability of an electrochemical system and interpret the measurement is to represent the data in a so-called Nyquist plot, by plotting the negative imaginary part versus real part of the complex impedance.

Electrochemical systems can be modeled using equivalent electric circuits. In polycrystalline solids, when a capacitor and a resistor are in connected in parallel, the result is a semi-circle in the Nyquist plot. The behaviour of many investigated systems, however, does not fit ideal resistors and capacitors. Therefore, replacing capacitors by constant phase elements (CPE) leads to better fitting results. From the fitting parameters, capacitance can be calculated. The values in magnitude of 10^{-12} F indicate bulk capacitance. Another type of capacitance, that can be determined by impedance spectroscopy is grain boundary capacitance with values in the 10^{-11} - 10^{-8} F range [49, 50].

3. Experimental

All reagents were purchased from commercial suppliers and used without further purification. The used chemicals and solvents are listed in the following table.

Table 4: Listed chemicals and solvents used during the experiments

Name	Supplier	CAS-Number
Zirconium(IV) chloride $\geq 99.5\%$ trace metals basis	Sigma-Aldrich	10026-11-6
Terephthalic acid 98%	Sigma-Aldrich	100-21-0
2-Aminoterephthalic acid 99%	Sigma-Aldrich	10312-55-7
2,5-Dihydroxyterephthalic acid 97%	abcr GmbH	610-92-4
Hydrochloric acid fuming 37 %	Merck KGaA	7647-01-0
N,N-Dimethylformamide $\geq 99.5\%$	Carl Roth	68-12-2
Selectipur [®] Dimethylcarbonate, anhydrous	Merck KGaA	616-38-6
1-Ethyl-3-methylimidazolium bis(fluorosulfonyl)imide	proionic	235789-75-0
Tetrahydrofuran, anhydrous, 99.8+%, unstab.	Alfa Aesar	109-99-9
Methanol	Merck KGaA	67-56-1
3-Methyl-3-pentanol	Sigma-Aldrich	77-74-7

3.1. Synthesis of UiO-66, UiO-66-NH₂ and UiO-66-(OH)₂

UiO-66, UiO-66-NH₂ and UiO-66-(OH)₂ were synthesized using the same procedure, as it was proposed by Katz *et al.* [35] and scaled up to 50 mL. For each MOF, a 100 mL screw-cap bottle was used as reaction vessel. ZrCl₄ was pre-dissolved in DMF and HCl (5:1 volume ratio) by ultrasonic treatment for 15 minutes and mixed with the respective benzene-dicarboxylic acid (see Figure 8), **a**, **b**, **c**. They were mixed in a molar ratio of 1:1.4 where **a**, **b** and **c** were pre-dissolved in 33.3 mL DMF by 15 minutes ultrasonic treatment. Each of the solutions had a different color. The mixtures were sonicated for 10 minutes and the closed bottles were put in a pre-heated drying cabinet at 80 °C overnight. For each solution the corresponding MOF was precipitated overnight. The mixtures were centrifuged and the solvent was decanted. The remaining particles were washed three times with 15 mL DMF.

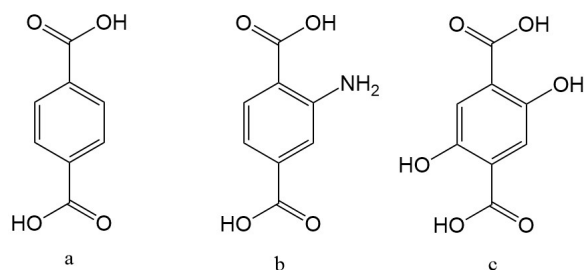


Figure 8: Structure of ligands used in the synthesis of UiO-66 derivatives: **a** terephthalic acid, **b** 2-aminoterephthalic acid, **c** 2,5-dihydroxyterephthalic acid



Figure 9: The MOFs after drying at 120 °C

After washing, the MOF particles were dried in a muffle furnace at 120 °C over night. UiO-66 and UiO-66-NH₂ were activated by drying under vacuum (1×10^{-3} mbar) at 120 °C for 4 hours, whereas UiO-66-OH₂ was vacuum dried at the same temperature for 5h. The purpose of activation is to free the pores from solvent and dehydration of the cluster core. Small amounts of the MOFs were taken for the XRD and BET analysis. The BET analysis was performed at 150 °C (UiO-66, UiO-66-NH₂) and 100 °C (UiO-66-(OH)₂) and required previous solvent exchange. Under the assumption that there is still some DMF left in the pores, a washing process with methanol needed to be executed to remove the adsorbed DMF, which was undesirable in the highly sensitive BET measuring device. DMF cannot be removed below 160 °C during the degassing process and consequently leads to incorrect results.

3.2. Synthesis of Lithium 3-methyl-3-pentoxide

The 1 M Lithium 3-methyl-3-pentoxide solution was synthesized according to the patent Schwindeman et al. [51]. The reaction was carried out in argon atmosphere. The molar ratio of lithium metal to alcohol was 1.9:1. 2,614 g of lithium metal foil was cut in small pieces and scratched with a scalpel to remove the passive layer from the surface. They were put in 175,2 mL THF with 24,8 mL 3-methyl-3-pentanol in a round flask that was closed using Teflon sealing rings. The mixture was heated

under reflux at temperatures between 68 and 70 °C. The reaction started when H₂ evolution was observed. After 30 minutes the solution became yellow. As long as the gas development took place, the reaction mixture continued to be heated. Finally, after four days the reaction was over and the solution was filtered to remove unreacted lithium and stored in the glovebox.



Figure 10: The experimental set-up used for the synthesis of the lithium alkoxide

3.3. Grafting

The grafting of 3-methyl-3-pentoxide on the MOFs was carried out as follows. The ratio of the reactants was 100 mL alkoxide solution per 1 g activated MOF. The preparation was carried out in the glovebox. 250 mg of the MOF was put with 25 mL of the 1 M alkoxide solution in a Schlenk tube. Since the reaction needs to take place in the absence of air, a small piece of lithium metal was put into the Schlenk-type female joint cap to act as a scavenger for oxygen and water that might enter the reaction tube. The closed Schlenk tube was taken out from the glovebox and the reaction was performed in the fume hood. Three Schlenk tubes (one for each activated MOF) were fixed on a retort stand, covered with aluminium foil to prevent heat loss, and immersed into an oil bath. The reaction was carried out under heating at 60 °C for seven days. During the reaction time, the color of the solutions changed from pale yellow to red (UiO-66-alkoxide), intense yellow (UiO-66-NH₂-alkoxide) and orange (UiO-66-(OH)₂-alkoxide), respectively. After seven days, the Schlenk tubes were transferred to the glovebox and the suspensions were filled into glass vials. Afterwards the suspensions were centrifuged for 10 minutes at 2500 rpm. The clear solutions were decanted and the sedimented product was washed with dry THF in the glovebox and centrifuged again for 10 minutes. The washing process with THF was repeated four times. The products were dried at 80 °C for three hours and afterwards at 120 °C for one hour. Very small amounts of each powder were taken for the XRD-Analysis to verify if the crystalline structure

remained after the grafting process.

3.4. Preparation of ionogels

One ionogel was prepared from each of the three activated pristine MOFs and each of the grafted products.

The exact compositions and concentrations are shown in Table 5 and Table 6. The density of [EMIM][FSI] is 1.39 g mL^{-1} .

Table 5: Names and abbreviations of the prepared ionogels

Ionogel	Sample
EMIM-FSI@UiO-66	A
EMIM-FSI@UiO-66-Li3m3p	B
EMIM-FSI@UiO-66-NH ₂	C
EMIM-FSI@UiO-66-NH ₂ -Li3m3p	D
EMIM-FSI@UiO-66-(OH) ₂	E
EMIM-FSI@UiO-66-(OH) ₂ -Li3m3p	F

Table 6: Composition of the 6 ionogels: The rows are displayed in three different colors, with the red rows corresponding to the UiO-66, UiO-66-NH₂ is shown in blue and the quantities of the UiO-66-OH₂ based ionogels are highlighted in green.

Sample	pristine MOF [mg]	modified MOF	EMIM-FSI [μL]
A	70	-	21.6
B	-	70	21.6
C	70	-	21.6
D	-	70	21.6
E	70	-	21.6
F	-	70	21.6

Unfortunately, direct mixing was not possible because of the large difference in volume and consequently poor distribution. In order to achieve an even distribution, the ionic liquid and the salt-ionic liquid mixtures were dissolved in 1.5 mL dimethyl carbonate each and the respective MOF was added. The suspension was agitated thoroughly and left in the glovebox for the next 4 days. Then, the dimethyl carbonate was evaporated and the sample dried under vacuum.

Dimethylcarbonate is much more volatile in respect to the ionic liquid, thus it was easily removed from the mixture during vacuum drying at $100 \text{ }^\circ\text{C}$. [EMIM][FSI] has a very high boiling point, so it was not removed by the drying process.

The particles did not show any change in color, but the consistency of the powder changed after treatment with ionic liquid. The soaked MOFs were pressed into pellets in the glovebox at a pressure of 0,25 tons. The diameter of each pellet was 5 mm. The pellets were coated on both sides with 100 nm gold. Consequently, coin cells were assembled in the glovebox to analyse the MOFs with impedance spectroscopy.

4. Results and discussion

4.1. Powder XRD and BET Analysis

The MOFs were characterized by XRD analysis. The XRD pattern of each MOF (see Figure 11) shows crystalline structure after activation. The two characteristic peaks occur at very small angles.

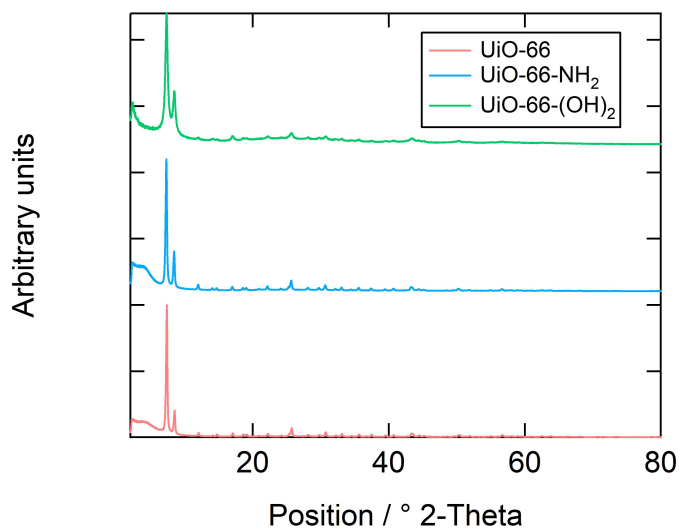


Figure 11: XRD patterns of UiO-66, UiO-66-NH₂ and UiO-66-(OH)₂ after activation confirm the crystal structure

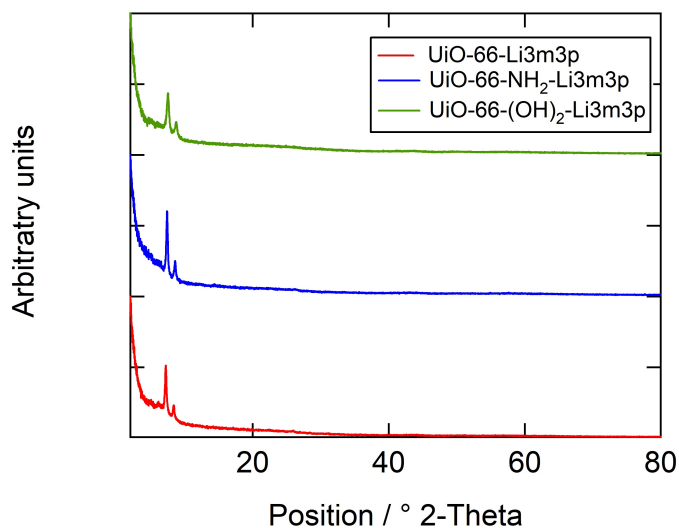


Figure 12: XRD patterns of UiO-66-Li3m3p, UiO-66-NH₂-Li3m3p and UiO-66-(OH)₂-Li3m3p

After the grafting process, the crystalline structure was retained (Figure 12). The XRD analysis suggests that UiO-66, UiO-66-NH₂ and UiO-66-(OH)₂ have cubic framework structure and crystallize in the Fm-3m space group, as reported in the studies [35, 36, 39]. The obtained and refined lattice parameters are very similar to those available in literature.

Table 7: Obtained lattice parameters

Lattice constant	UiO-66	UiO-66-NH ₂	UiO-66-(OH) ₂
a [Å]	20.725	20.778	20.820

UiO-66, UiO-66-NH₂ and UiO-66-(OH)₂ are iso-structural, the lattice parameters only show a slight difference. Using the Scherrer equation and assuming round crystallites, the approximate average crystallite size were estimated (standard sample LaB₆) and have the following values:

Table 8: Average crystallite size of the derivative MOF nanoparticles

Average size	UiO-66	UiO-66-NH ₂	UiO-66-(OH) ₂
r [nm]	45	50	20

In most practical applications it is preferable to have small particles, because through the pores of the MOF the diffusion of species is easier [52]. The synthesis method has a huge impact on the crystallite [39]. The approach of Katz et al. [35] is suitable for achieving small crystallites. The use of ultrasonification during the preparation of UiO-66 and its derivatives allows accelerated nucleation at ambient pressure. The obtained particles are more uniform and smaller than in other synthesis methods, such as the solvothermal synthesis [39, 53]. The addition of water also increases the rate of growth, which leads to shorter crystallization time and smaller particles as obtained in the experiment (Table 7 and 8).

The active surface area of the MOFs was determined by BET (Brunauer-Emmett-Teller) analysis. The results were compared with the values seen in literature [35] and show similarities. The porosity and average pore size (Table 9) show high values compared to the theoretical parameters, estimated via computational simulations. The reason is the absence of a small fraction of linkers because of the addition of concentrate hydrochloric acid during the preparation [35].

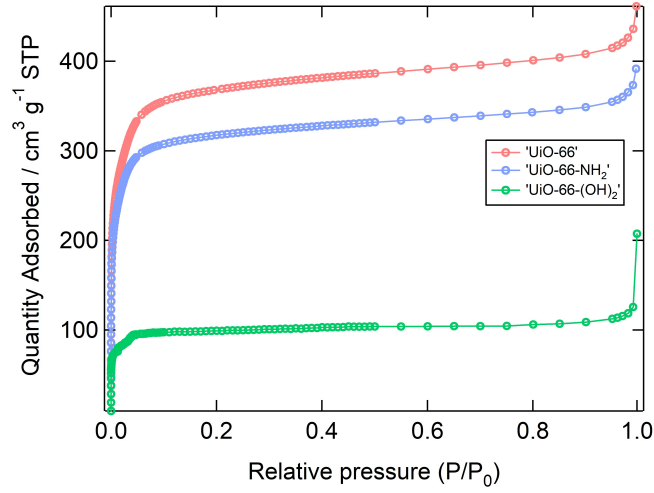


Figure 13: Nitrogen adsorption isotherms at 77 K used for the determination of BET specific surface area.

Table 9: Comparison of obtained results and values in literature

S_{BET} [m^2/g]	Literature	Obtained
UiO-66	1580	1520
UiO-66-NH ₂	1200	1297
UiO-66-(OH) ₂	560	441

The active surface area decreases with the presence and number of functional groups on the organic linker. The estimated pore size in diameter for each MOF is shown in Figures 14-15 and the values are given in Table 10.

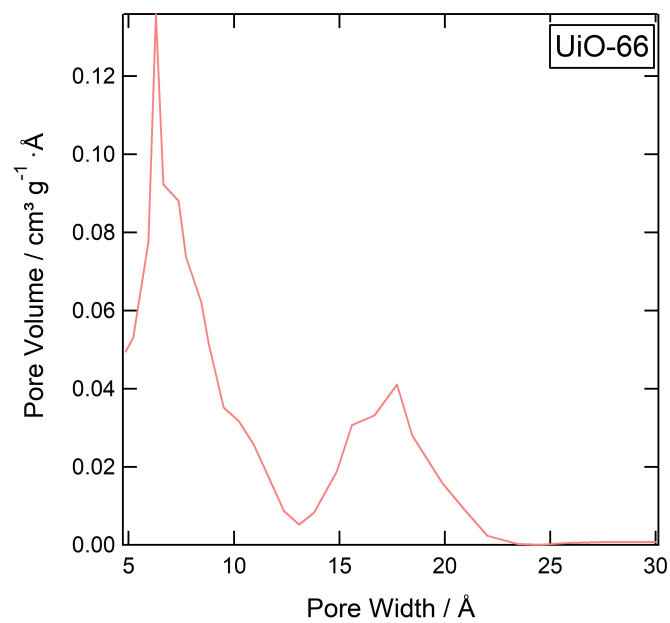


Figure 14: Pore size distribution of UiO-66

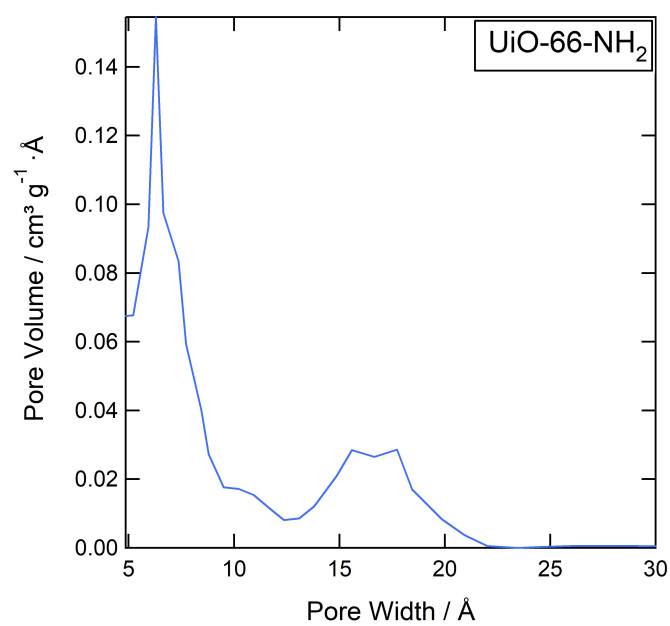


Figure 15: Pore size distribution of UiO-66-NH₂

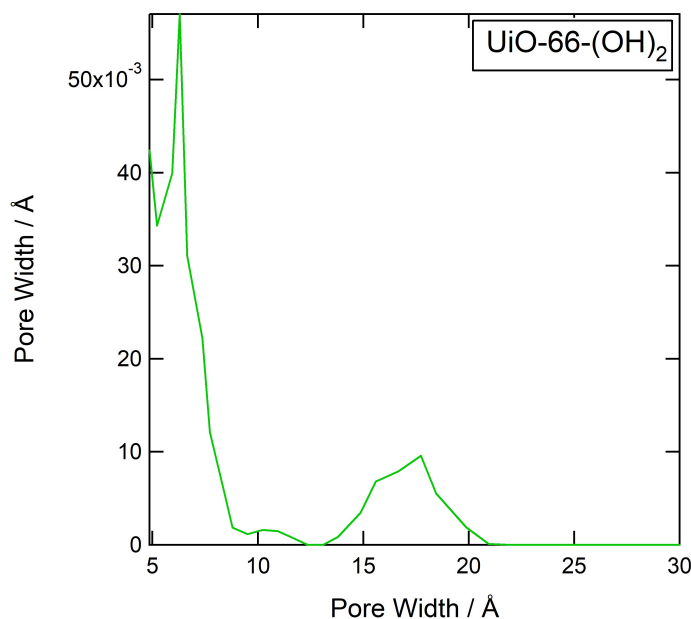


Figure 16: Pore size distribution of UiO-66-(OH)₂

Table 10: Measured average pore size

Diameter [Å]	Tetrahedral pore	Octahedral pore
UiO-66	6.3	17.7
UiO-66-NH ₂	6.3	16.7
UiO-66-(OH) ₂	6.3	17.7

UiO-66, UiO-66-NH₂ and UiO-66-(OH)₂ have insulating nature, but are well suited as solid supports for the immobilization of ionic liquids. As the PXRD and BET analysis shows a successful synthesis, high specific surface areas and porosities, the MOFs are suitable scaffolds for immobilization of the EMIM-FSI as pore sizes appear to be large enough.

First, UiO-66, UiO-66-NH₂ and UiO-66-(OH)₂ were soaked with 30 wt.% ionic liquid EMIM-FSI (1-Ethyl-3-methylimidazolium bis(fluorosulfonyl)imide) which was previously diluted with dimethylcarbonate (DMC). DMC was removed in a drying process and a powder that appears dry with very good deformability was obtained.

The size of the bis(fluorosulfonyl)imide (FSI) anion is 5.4 Å according to the literature [54] and the EMIM cation 7.6 Å [55] (Figure 8). Very likely, the ionic liquid was trapped in the MOF pores. The excess of the ionic liquid was adsorbed on the external surface of the MOF particles.

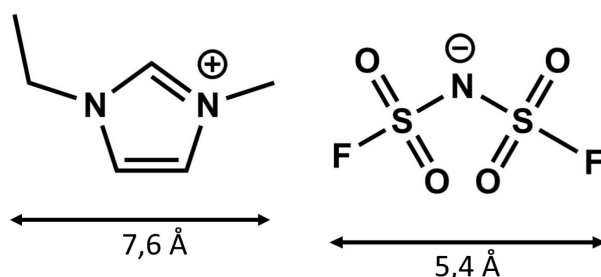


Figure 17: The size of EMIM cation (left) and FSI anion (right)

According to the BET results, the pores are wide enough to trap the ionic liquid. The fact that the performed synthesis method caused linker defects further supports this statement. The successful confinement of the EMIM-FSI in the pores of UiO-66, UiO-66-NH₂ and UiO-66-(OH)₂ was confirmed by ATR (attenuated total reflection) infrared spectroscopy.

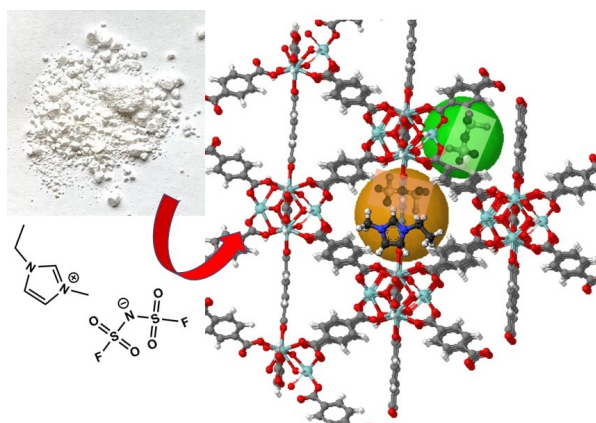


Figure 18: The illustration shows confinement of EMIM-FSI in the pores (orange and green sphere) of the UiO-66 structure

4.2. ATR-FTIR

Fourier transform IR spectra of two ionogels (UiO-66@EMIM-FSI and UiO-66-NH₂@EMIM-FSI) and MOFs (UiO-66 and UiO-66-NH₂) were recorded in the range from 4000 to 600 cm⁻¹ with attenuated total reflection (ATR) technique. The following absorbance spectra are baseline corrected and normalized. To get a better overview, the wavenumbers ν from 4000-1850 cm⁻¹ containing non relevant data were cut out from the following spectra. The comparison of ATR spectra of pure EMIM-FSI and immobilized EMIM-FSI in the pores of UiO-66 is shown in Figure 19. UiO-66 shows strong bands at 1390 and 1580 cm⁻¹, which are attributed to

asymmetric and symmetric stretching of the O-C-O bond in the BDC linker. The band at 1665 cm^{-1} is representing the C=O bond stretching vibrations of the BDC linker. The weak band at 1500 cm^{-1} is related to the vibration of the C=C bond in the benzene ring. Considering the ionic liquid, the FSI anion generates bands at 725 and 825 cm^{-1} attributed to symmetric and asymmetric S-N-S bond stretching and bands at 1100 and 1165 cm^{-1} corresponding to the SO_2 asymmetric stretching and C-F asymmetric stretching, respectively.

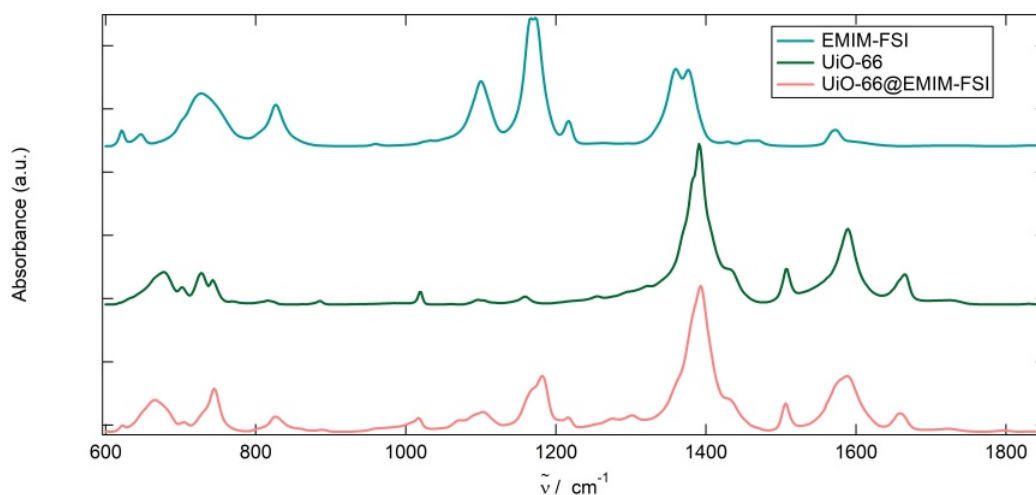


Figure 19: Absorption IR-spectra of UiO-66 (green), ionic liquid (blue-green) and ionic liquid that is trapped in the pores of UiO-66 (red).

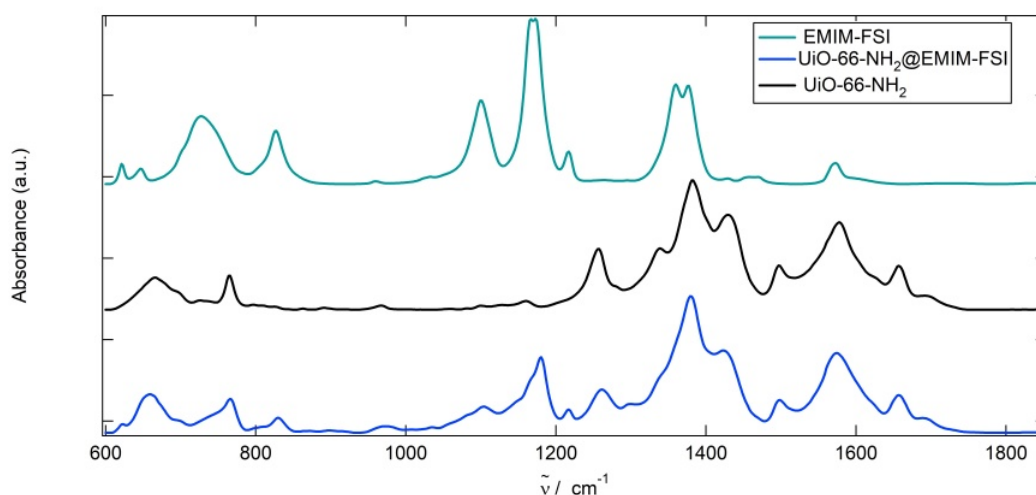


Figure 20: Absorption IR-spectra of UiO-66-NH₂ (black), ionic liquid (blue-green) and ionic liquid that is trapped in the pores of UiO-66-NH₂ (blue).

Finally, when comparing the $\nu(\text{S-N-S})$ and $\nu(\text{SO}_2)$ of the pure and the trapped ionic liquid (see Figure 21 and 22), blue shifts are observed at the spectrum of ionic

liquid within the confines of the pores. This indicates strong interactions between the FSI anion and the zirconium center of the MOF.

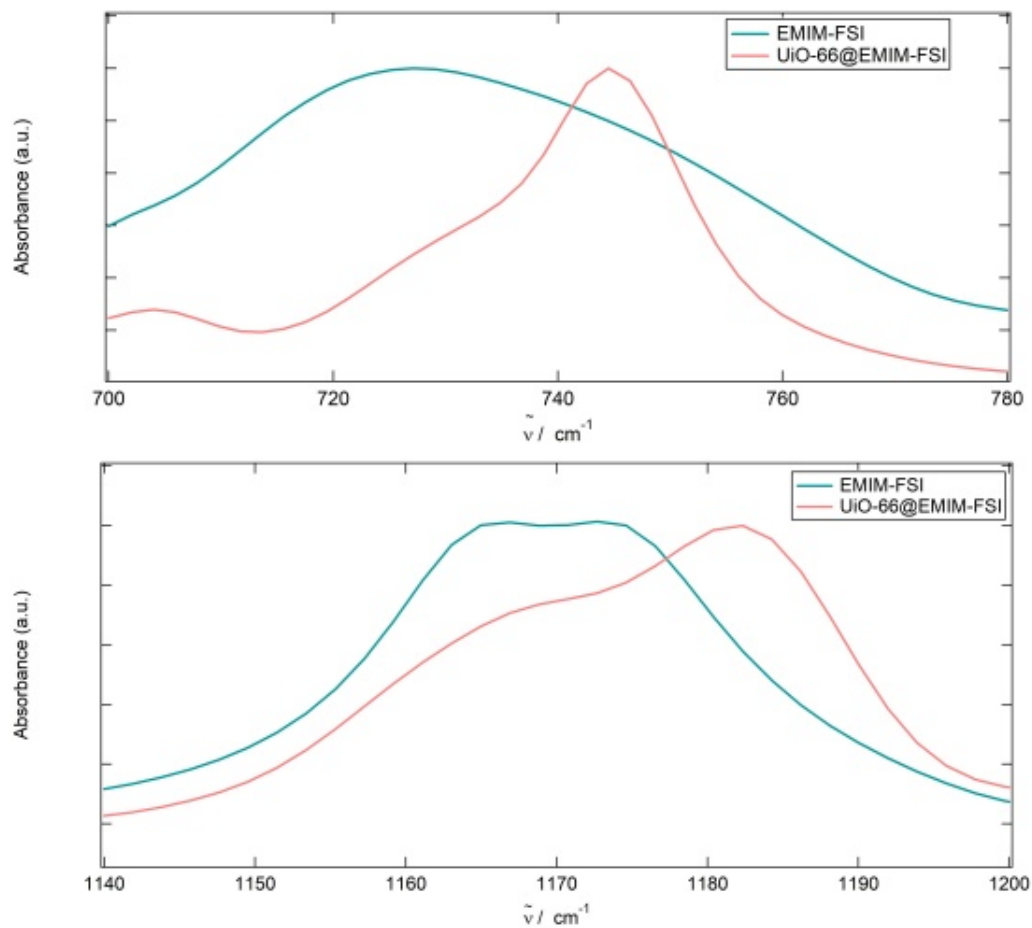


Figure 21: IR-Absorption bands $\nu(\text{S-N-S})$ (top) and $\nu(\text{SO}_2)$ (bottom) of the pure ionic liquid (blue-green) and the ionic liquid which is trapped in the pores of UiO-66 (red).

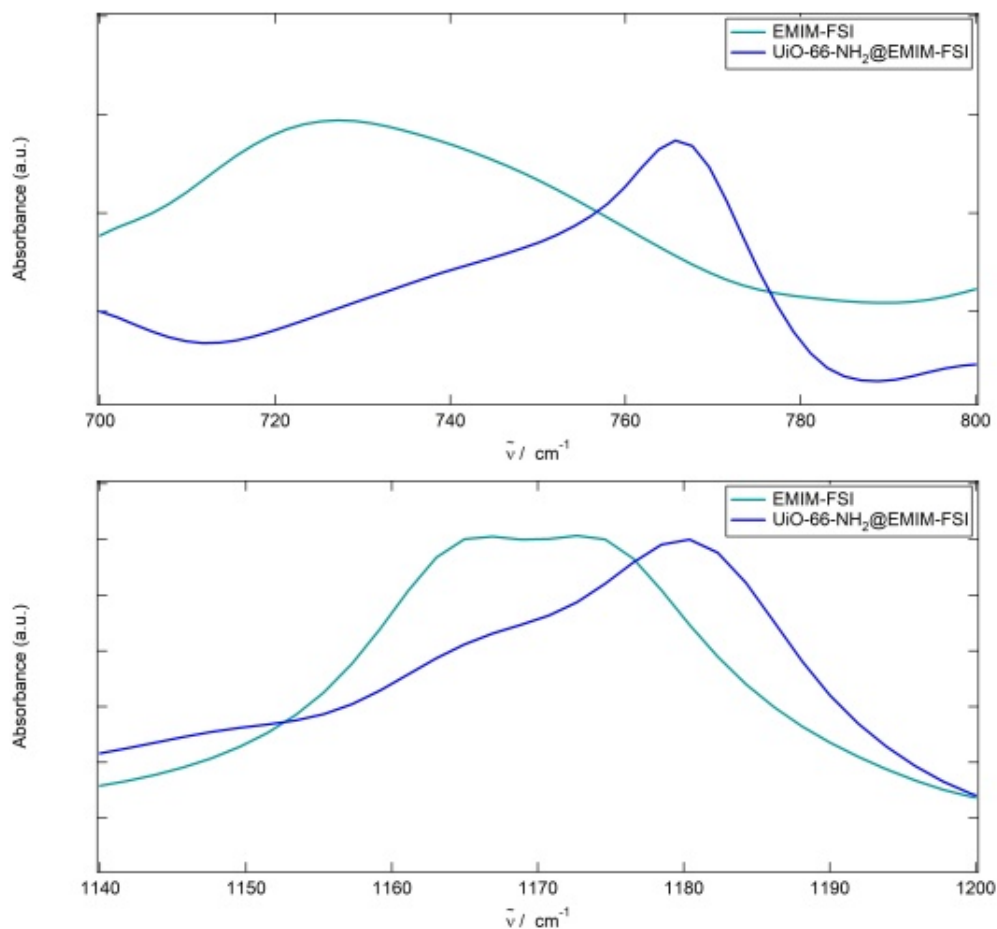


Figure 22: IR-Absorption bands $\nu(\text{S-N-S})$ (top) and $\nu(\text{SO}_2)$ (bottom) of the pure ionic liquid (blue-green) and the ionic liquid which is trapped in the pores of UiO-66-NH₂ (blue).

In Figure 20 there is an additional peak appearing at 1255 cm^{-1} ($\text{C}_{\text{ar}}\text{-N}$) related to the amino group attached to the BDC linker. The spectrum of the ionogel shows a shift of $\nu(\text{S-N-S})$ and $\nu(\text{SO}_2)$ to higher wavenumbers as well, with respect to the pure ionic liquid spectrum. To conclude, the blue shift of the relevant bands proves the confinement of the ionic liquid in the pores of the UiO-66 and UiO-66-NH₂ and consequently, a successful synthesis of the ionogel [56].

4.3. Impedance spectroscopy

The impedance of the prepared ionogels was measured with impedance spectroscopy to obtain information about conductivity. The measurements were performed with a Novocontrol Concept 80 impedance spectrometer over a temperature range of -80°C to 100°C and a frequency range of 10 mHz to 10 MHz. The applied voltage was 10 mV in terms of V_{RMS} , which stands for *Root-Mean-Square* voltage. The

software ZView was used for fitting the EIS data in accordance to the equivalent circuit for accurate determination of the values of capacitance and resistance.

4.3.1. Ionogels based on UiO-66

UiO-66 has an insulating nature and exhibits very low electronic/ionic conductivity. This property is attributed to the fact that UiO-66 is constructed from zirconium cations and redox-inactive ligands and cannot provide efficient routes for charge transport. The ionic liquid enables charge transport through the pores of the MOF and consequently increases the conductivity. Figure 23 shows the conductivity applied against the frequency and the Nyquist plot of the ionogel **A**. The DC plateau is seen at high temperatures in the middle frequency range and at room temperature (and lower temperatures) in the lower frequency range. The DC plateau conductivity is *approx.* $2 \times 10^{-7} \text{ S cm}^{-1}$ at $100 \text{ }^\circ\text{C}$ and $1.5 \times 10^{-9} \text{ S cm}^{-1}$ at $20 \text{ }^\circ\text{C}$. A weak scattering of conductivity can be seen at temperatures below $0 \text{ }^\circ\text{C}$. This is partly due to the fact that the conductivity is extremely low and the measured values are at the upper limit of impedance which is measurable by the instrument.

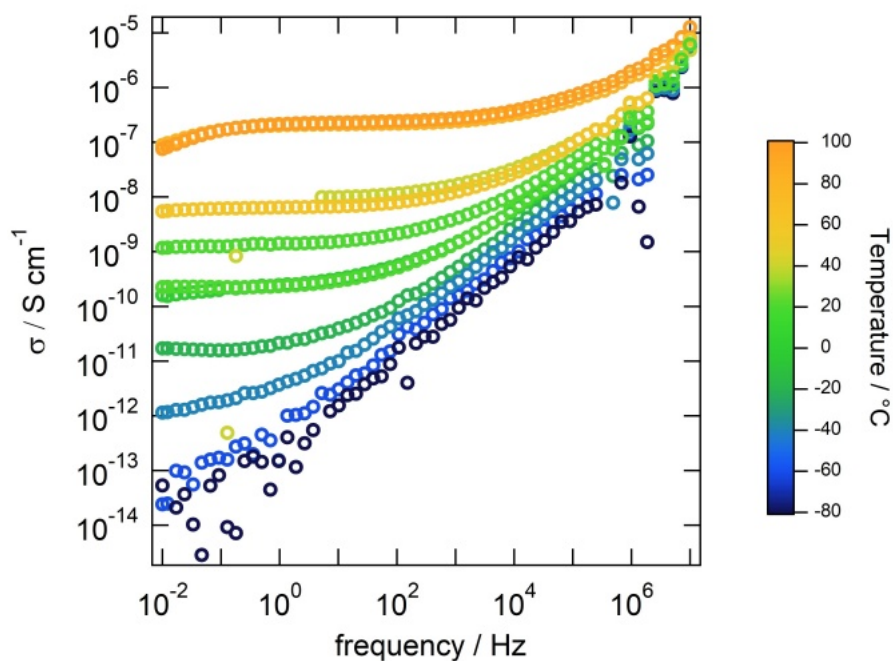


Figure 23: Conductivity isotherms of the UiO-66@EMIM-FSI (ionogel **A**)

Ionogel **B** (see Figure 24) is the grafted version of ionogel **A** and shows an increase in conductivity of three orders of magnitude. The DC plateau conductivity is *approx.* $4 \times 10^{-5} \text{ S cm}^{-1}$ at $100 \text{ }^\circ\text{C}$ and $4 \times 10^{-6} \text{ S cm}^{-1}$ at $20 \text{ }^\circ\text{C}$.

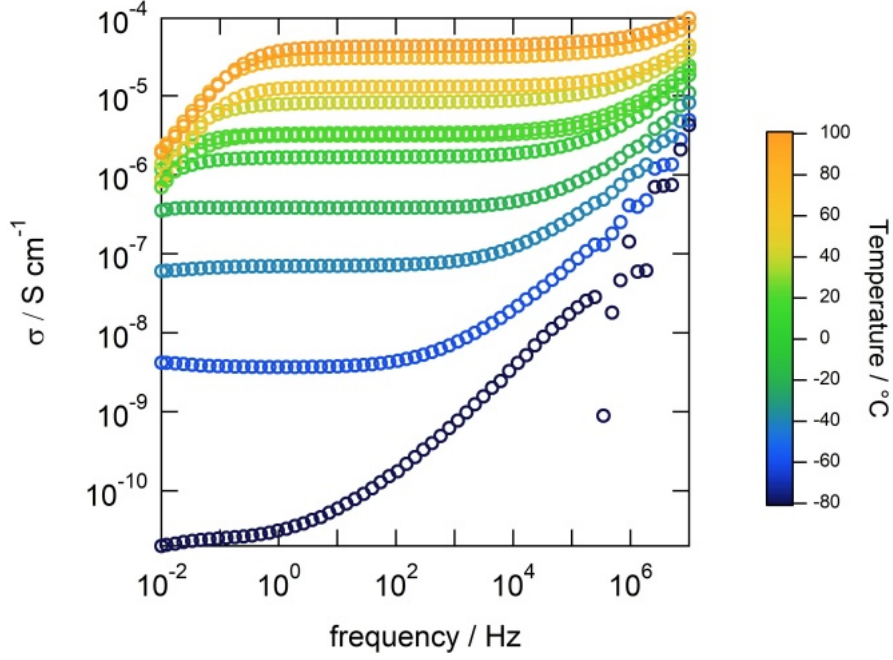


Figure 24: Conductivity isotherms of the UiO-66-Li3m3p@EMIM-FSI (ionogel **B**)

The Nyquist plot of sample **A** and the used equivalent circuit is shown in Figure 25. The equivalent circuit is composed of a resistor and a constant phase element (CPE) connected in parallel. To fit the semicircle a CPE is used rather than a capacitor, because the capacitance of real ionic conductors does not behave ideally. For estimation of true capacitance, three parameters were involved, namely CPE-T (pseudo capacitance), CPE-P (related to the semi-circle) and R (resistance). Two parameters were varied to fit the semi-circle, while one of them was fixed till the fitting function matched the semi-circle. The following function is applied for calculation of the true capacitance:

$$C = R^{(1-n)/n} + Q^{1/n}$$

where R is the resistance, Q is the CPE-T and the exponent n is the CPE-P parameter. The measured capacitance for sample **A** is *approx.* 30 pF, which indicates bulk conductivity according to literature [57].

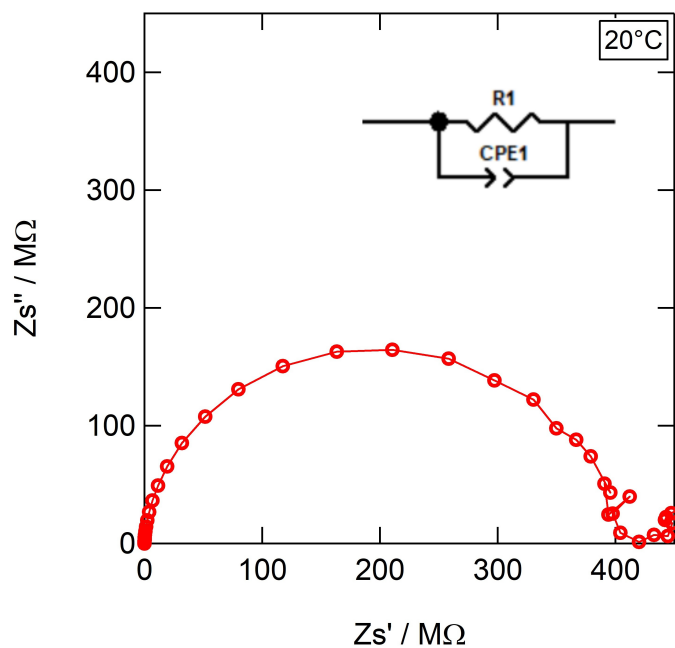


Figure 25: The Nyquist plot of the UiO-66@EMIM-FSI (ionogel **A**). The equivalent circuit used for fitting the data is attached to the Nyquist plot.

Ionogel **A** exhibits a very high resistance, although it is not certain whether it is poor ionic conduction or also some electronic conduction. Ionogel **B** shows resistance in the $k\Omega$ range and a capacity of 23 pF which indicates bulk conductivity as well. Obviously, since the ionogel **A** does not contain lithium ions, this accounts only for the transport of ionic liquid ions in the pores. In the case of ionogel **B**, the conductivity is much better, very likely due to the mobile Li^+ ions.

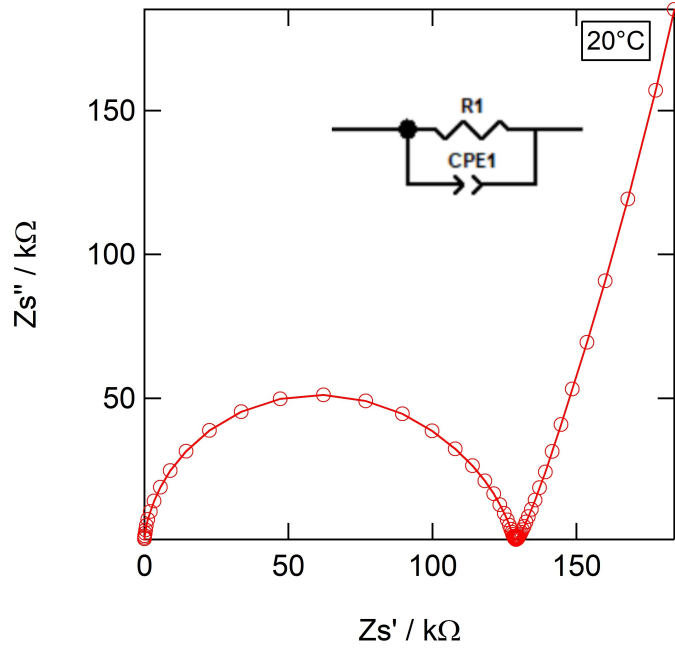


Figure 26: The Nyquist plot of the UiO-66-Li3m3p@EMIM-FSI (ionogel **B**) and the equivalent circuit used for fitting the data

The Arrhenius plot of the ionogel **A** is given in Figures 27. For determination of the activation energy E_a , one value was taken from the DC plateau at (almost) all measured temperatures and plotted logarithmically versus $1/T$ (K). In this way the thermal dependence of conductivity (see following equation) was linearized.

$$\sigma_{DC} = \frac{\sigma_0}{T} e^{\frac{E_a}{k_b T}}$$

In some cases, the lowest temperatures were not included because of the strong conductivity scattering. The slope of the linear fit is proportional to the activation energy.

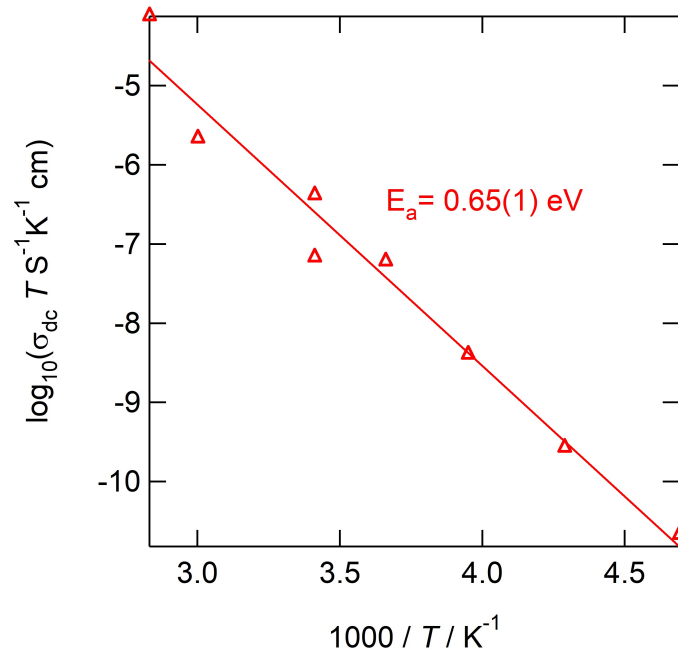


Figure 27: Arrhenius plot of ionogel **A**

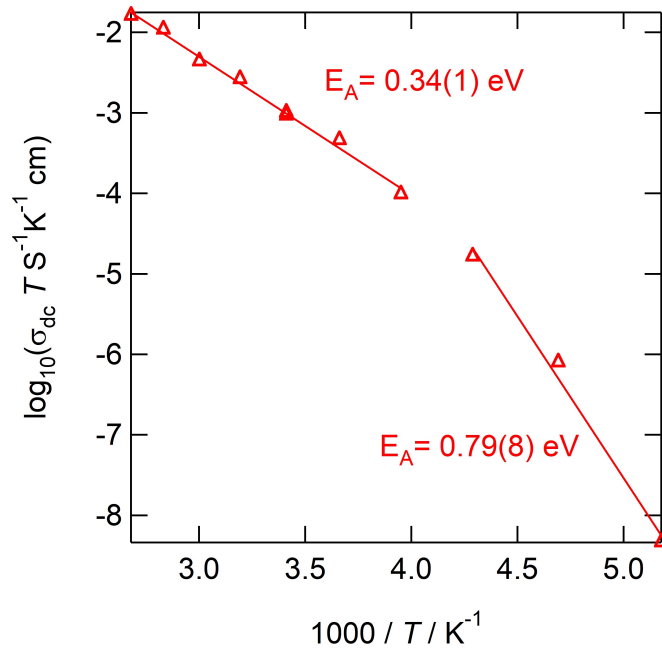


Figure 28: Arrhenius plot of ionogel **B**

The Arrhenius plot of ionogel **B** (Figure 28) shows two fits as a result of a change in slope at 0 °C, because of a possible phase transition or structural change of the

material.

4.3.2. Ionogels based on UiO-66-NH₂

Ionogel **C** exhibits similar conductivity as ionogel **A** at higher temperatures and lower conductivity at room temperature, which is unusual since the UiO-66-NH₂-based ionogel may provide some protons that are assumed to contribute to the total conductivity. Figure 29 shows the DC plateaus of **C** at $1.4 \times 10^{-7} \text{ S cm}^{-1}$ at 100 °C and $4.7 \times 10^{-10} \text{ S cm}^{-1}$ at 20 °C.

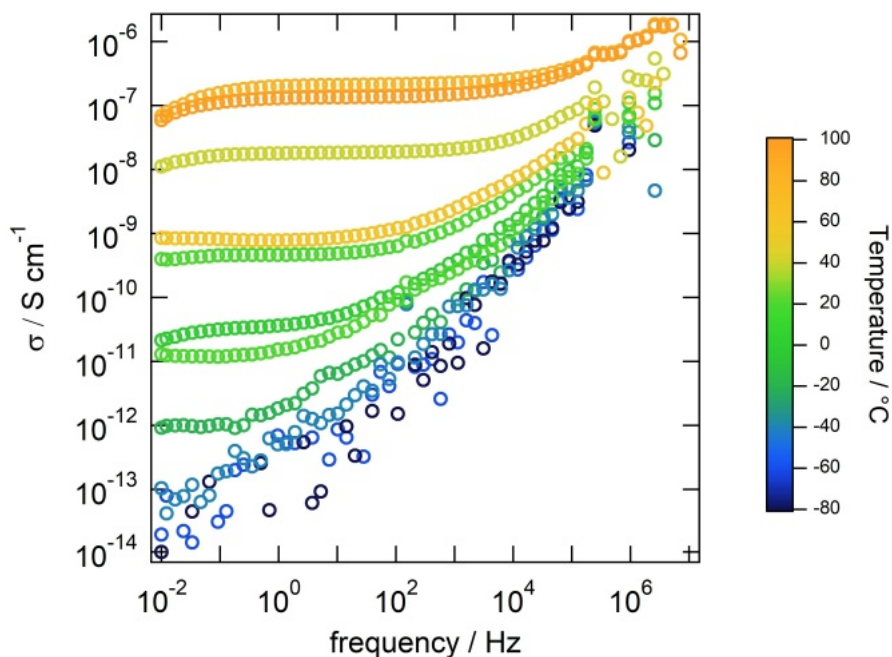


Figure 29: Conductivity isotherms of the UiO-66-NH₂@EMIM-FSI (ionogel **C**)

After grafting on UiO-66-NH₂, the conductivity increases drastically. In the conductivity isotherms of ionogel **D** (Figure 30) the DC Plateaus are located at $1.4 \times 10^{-4} \text{ S cm}^{-1}$ and 1.2×10^{-5} at 100 and 20 °C, respectively. The difference in conductivity at room temperature is five orders of magnitude. In addition, it can be assumed that the grafting process somehow contributed to the stability of the material, since the same values are observed on the heating- and on the cooling run. The conductivity scattering at low temperatures is almost negligible when compared to previous plots mainly due to the increase in conductivity also at low temperatures.

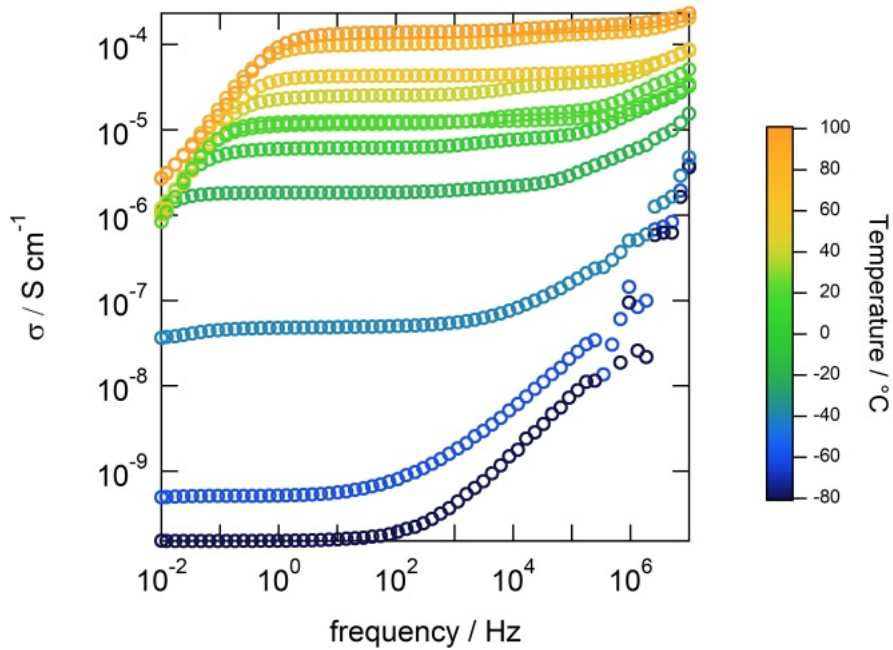


Figure 30: Conductivity isotherms of the UiO-66-NH₂-Li₃m₃p@EMIM-FSI (ionogel **D**)

After the post-modification of the MOF, the resistance moves from the $G\Omega$ into the $k\Omega$ range. In Figure 30 two DC Plateaus can be seen at temperatures above $-20\text{ }^{\circ}\text{C}$. Accordingly, there are two semicircles in the Nyquist plot of ionogel **D** which required a different equivalent circuit for fitting the EIS data (see Figure 32). The applied equivalent circuit is composed of two R-CPE circuits connected in series. By fitting of the semicircles, two capacitance values of 5300 and 20 pF were obtained. The modified material shows both types of transport, grain boundary- and bulk conductivity. The estimated capacitance value of the unmodified MOF soaked in IL (ionogel **D**, see Figure 31) is *approx.* 20 pF and indicates bulk conductivity.

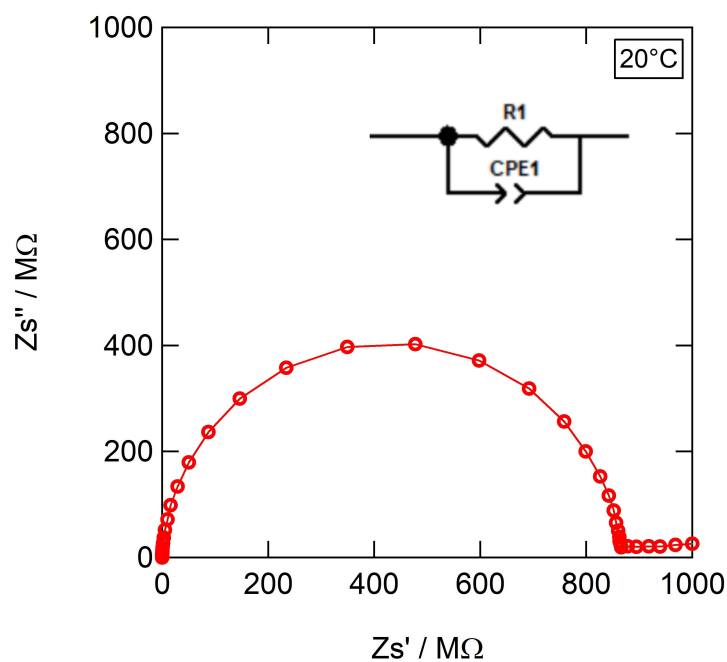


Figure 31: The Nyquist plot of the UiO-66-NH₂@EMIM-FSI (ionogel **C**) and the equivalent circuit used for fitting the data

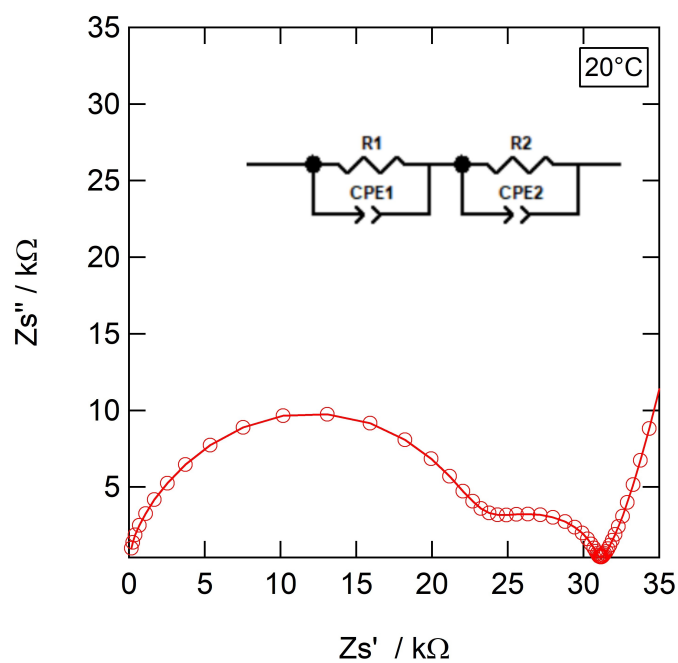


Figure 32: The Nyquist plot of the UiO-66-NH₂-Li₃m₃p@EMIM-FSI (ionogel **D**) and the equivalent circuit used for fitting the data

In Figure 33 the activation energy of ionogel **C** is shown but with high uncertainty

in slope. Figure 34 shows two fits as a result of a change in slope in the Arrhenius plot at $-20\text{ }^{\circ}\text{C}$ in Arrhenius plot. Due to the strong scattering in the Arrhenius plot of sample **C** it is not possible to make a clear evaluation and statement about the difference in activation energies.

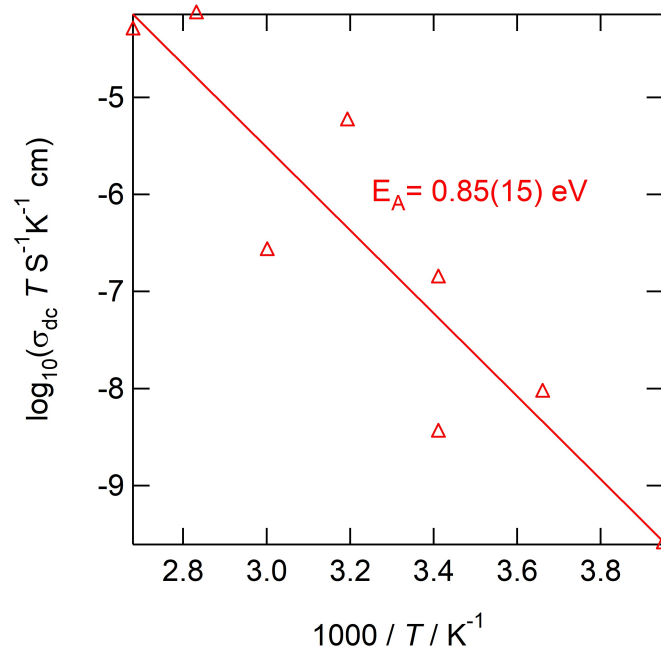


Figure 33: Arrhenius plot of ionogel **C**

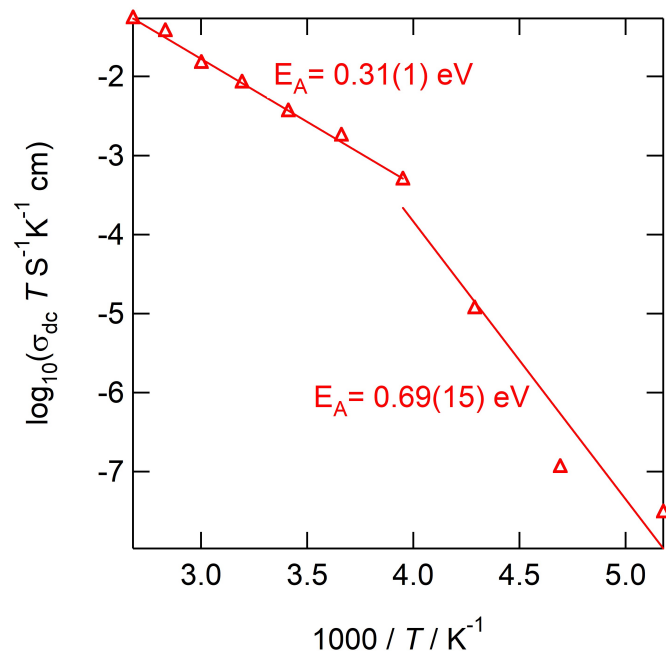


Figure 34: Arrhenius plot of ionogel **D**

4.3.3. Ionogels based on UiO-66-(OH)₂

Ionogel **E** (Figure 35) shows highest conductivity compared to the samples **A** and **C**. This was expected since the linker of the UiO-66-(OH)₂ probably provides more protons as it contains two hydroxyl-groups.

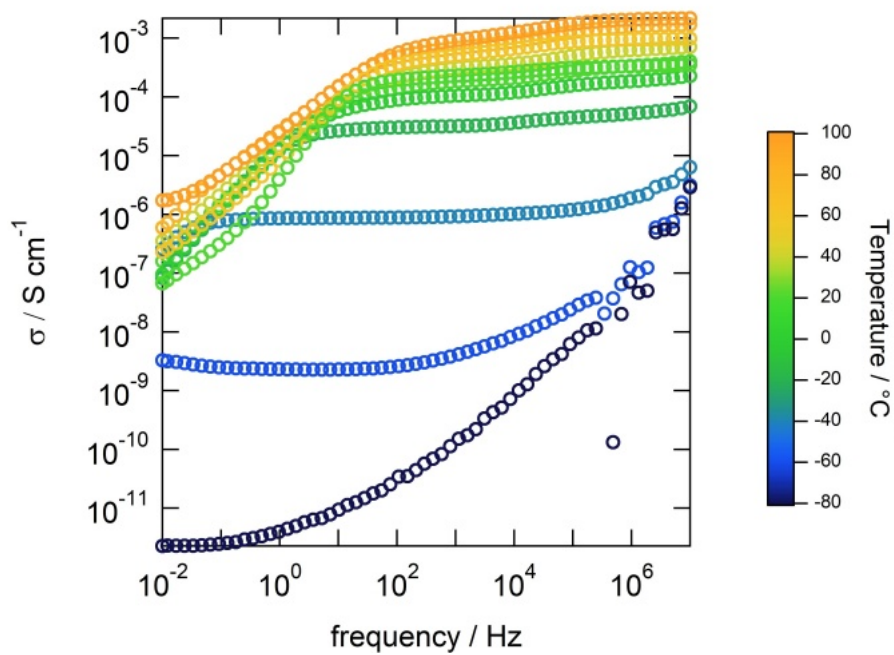


Figure 35: Conductivity isotherms of the UiO-66-(OH)₂@EMIM-FSI (ionogel **E**)

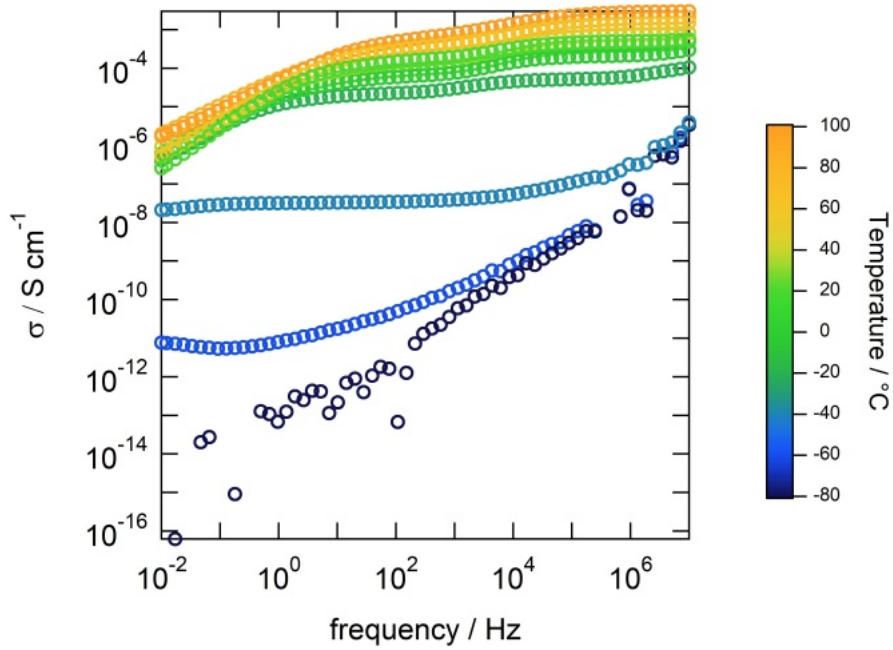


Figure 36: Conductivity isotherms of the UiO-66-(OH)₂-Li₃m₃p@EMIM-FSI (ionogel **F**)

In Figure 35 there are two DC Plateaus in the temperature range of 0 °C to 100 °C. The first DC Plateau at 100 °C lies at *approx.* 1×10^{-3} S cm⁻¹ and the second at *approx.* 2×10^{-3} S cm⁻¹. The DC Plateaus at 20 °C are located at 3.5×10^{-4} and 2.8×10^{-4} S cm⁻¹.

The post-modification with lithium alkoxide did slightly reduced the conductivity at temperatures above 0 °C and drastically at very low temperatures. The DC Plateaus in Figure 36 (ionogel **F**) can be seen at 3×10^{-3} and 6×10^{-4} S cm⁻¹ at 100 °C, and 7.3×10^{-4} and 1.5×10^{-3} S cm⁻¹ at 20 °C.

In the Nyquist plots of each ionogel two semi-circles can be observed. The capacitance values for ionogel **E** (Figure 37) are 8722 and 22 pF. This values indicate grain boundary and bulk conductivity. The capacitance values of 36025 and 22 pF for ionogel **F** are assigned to the grain boundary- and bulk conduction as well.

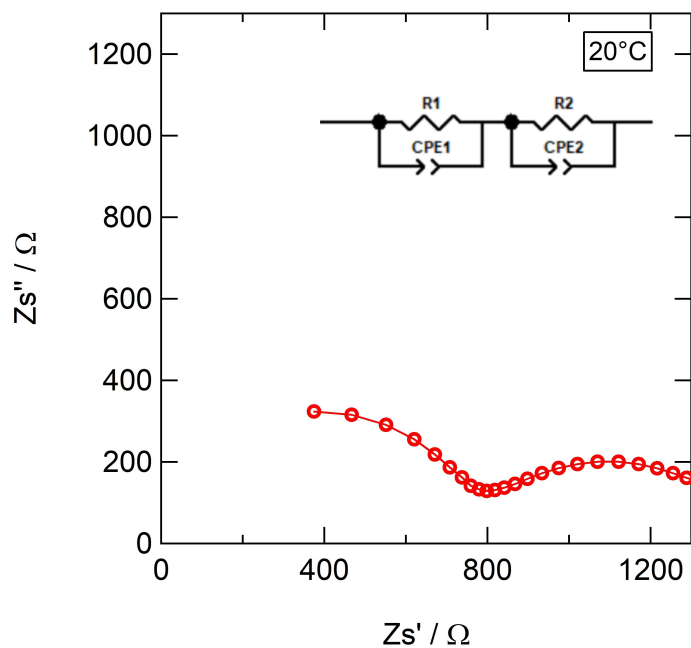


Figure 37: The Nyquist plot of the UiO-66-(OH)₂@EMIM-FSI (ionogel **E**) and the equivalent circuit used for fitting the data

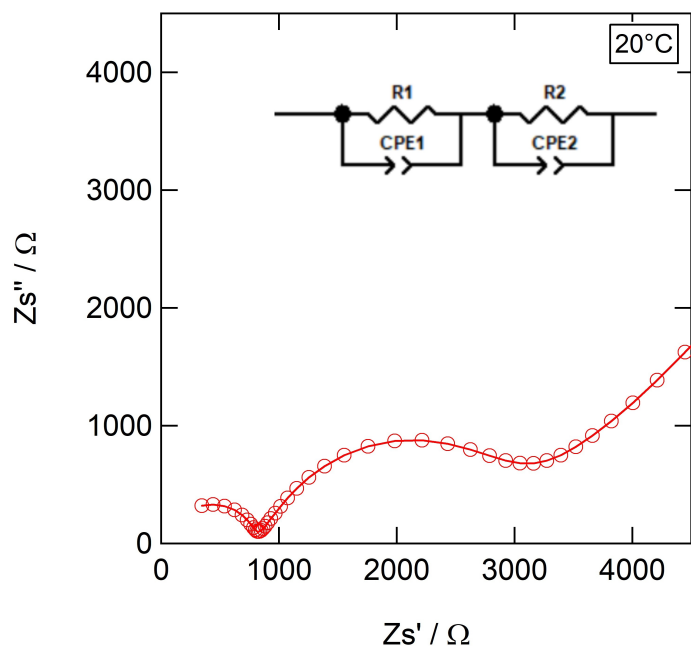


Figure 38: The Nyquist plot of the UiO-66-(OH)₂-Li3m3p@EMIM-FSI (ionogel **F**) and the equivalent circuit used for fitting the data

The Arrhenius plots of the UiO-66-(OH)₂-based ionogels are presented in Figures

39 and 40. The activation energy values of the ionogels **E** and **F** are similar. In each ionogel two regimes with different activation energies were observed as a result of a change in slope at -20°C .

A possible explanation of the decrease in conductivity after post-modification is the partial deprotonation of the hydroxy-groups, since the lithium alkoxide acts as a strong base instead of a nucleophile. The lithium ions are probably strongly attracted to the deprotonated hydroxy-groups of the linker which reduces their mobility. However, it is not clear if the protons or lithium ions are responsible for the conduction.

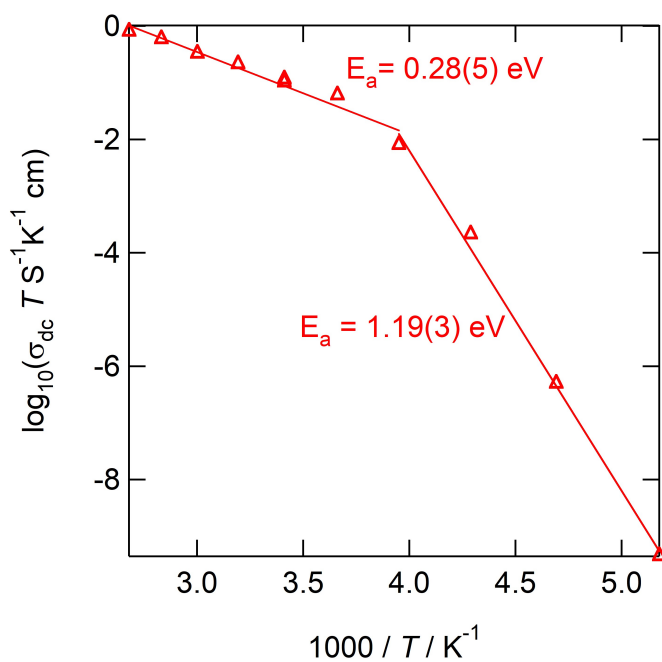


Figure 39: Arrhenius plot of ionogel **E**

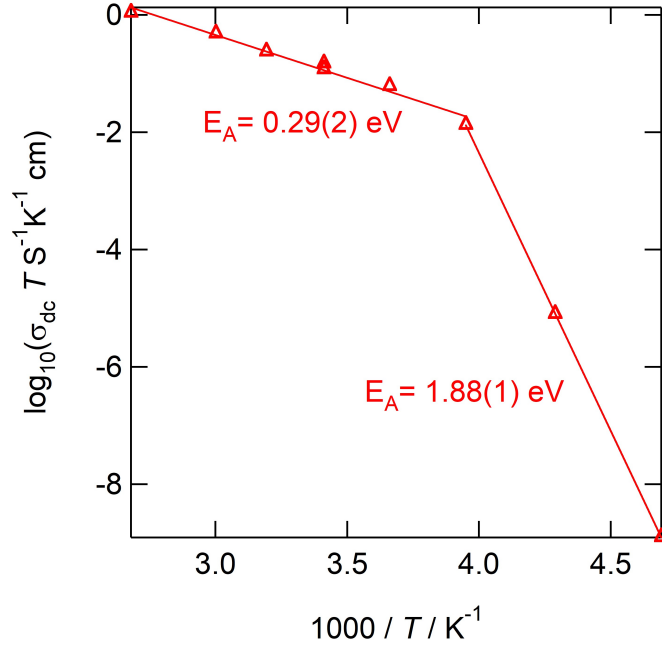


Figure 40: Arrhenius plot of ionogel **F**

All values for conductivity and capacitance are once again listed in the following table.

Table 11: Activation energy, conductivity- and capacitance values of the ionogels

Ionogel	$\sigma_{DC, 100 \text{ } ^\circ C} [S \text{ cm}^{-1}]$	$\sigma_{DC, 20 \text{ } ^\circ C} [S \text{ cm}^{-1}]$	$E_a [eV]$	Capacitance [pF]
A	2×10^{-7}	1.5×10^{-9}	0.65(1)	30
B	4×10^{-5}	4×10^{-6}	0.34(1), 0.79(8)	23
C	1.4×10^{-7}	4×10^{-10}	0.85(15)	20
D	1.4×10^{-4}	1.2×10^{-5}	0.31(1), 0.69(15)	5300, 20
E	$1 \times 10^{-3}, 2 \times 10^{-3}$	$3.5 \times 10^{-4}, 2.8 \times 10^{-4}$	0.28(5), 1.19(3)	8722, 22
F	$3 \times 10^{-3}, 6 \times 10^{-4}$	$1.5 \times 10^{-3}, 7.3 \times 10^{-4}$	0.29(2), 1.88(1)	36025, 22

5. Conclusion

Three isostructural MOFs were synthesized and post-modified with lithium alkoxide. Since most of the MOFs exhibit very low ionic conductivity, postmodifying the metal cluster or organic linker, and incorporation of guest molecules into the pores can improve the conductivity. In this work, UiO-66 and its derivatives were grafted with lithium 3-methyl-3-pentoxide. The alkoxide attached probably to the zirconium cluster. This mechanism is described more in detail by Ameloot *et al.* [36].

Ionic liquid [EMIM][FSI] was added to the pristine and modified MOFs to mediate the proton or lithium ion transport. The IL was previously solved in DMC and then added to the MOFs which is an effective and common strategy of impregnation of ILs into MOFs [58]. This way, six different ionogels were prepared. The successful synthesis of the MOFs was verified by PXRD and BET. The crystalline structure of the MOFs was preserved after post-modification which was confirmed by PXRD. The ATR-IR measurements proved the confinement of the ionic liquid in the pores of the MOFs. The peaks from the S–N–S and O=S=O vibrations experienced a blue shift, which is a result of relatively strong interactions between the zirconium center and N or S atoms of the FSI anion. Raman spectroscopy can be applied for additional informations about the specific interactions between the FSI anion and metal cluster of the MOF. The FSI anion is immobilized by the attractive force to the metal site leaving free cations in the pores. The ionic conductivity was investigated by impedance spectroscopy. The EIS measurements showed that the ionogel made of UiO-66-(OH)₂ has the highest ionic conductivity. After postmodifying the conductivity slightly decreased. Nevertheless, grain boundary conduction has a great contribution to the electrical behaviour of the UiO-66-(OH)₂-based ionogels. The UiO-66-based ionogels do not show a sufficiently high ionic conductivity for solid electrolyte applications. A great improvement in conductivity was achieved after post-modification of UiO-66-NH₂. The ionogel made of the grafted UiO-66-NH₂ exhibits a ionic conductivity of 1.2×10^{-5} S cm⁻¹ at 20 °C which is in the performance range of polymer electrolytes. The grafting process was successful, but the material still does not satisfy the requirements of SSEs for future battery generations. UiO-66 provides small pores in comparison to many other MOFs. The pore size determines the quantity and mobility of charge carriers which affects directly on conductivity. The degree of grafting and more information about the conduction pathways can be investigated by ⁷Li NMR. FTIR can provide more information about structural changes that occur due to cluster dehydration and subsequent grafting.

References

- [1] Taehoon Kim et al. “Lithium-ion batteries: outlook on present, future, and hybridized technologies”. In: *Journal of Materials Chemistry A* 7.7 (2019), pp. 2942–2964.
- [2] Kaifeng Yu et al. “High-capacity activated carbon anode material for lithium-ion batteries prepared from rice husk by a facile method”. In: *Diamond and Related Materials* 86 (2018), pp. 139–145.
- [3] Wen Liu et al. “Nickel-rich layered lithium transition-metal oxide for high-energy lithium-ion batteries”. In: *Angewandte Chemie (International ed. in English)* 54.15 (2015), pp. 4440–4457.
- [4] Jagjit Nanda, Chongmin Wang, and Ping Liu. “Frontiers of solid-state batteries”. In: *MRS Bulletin* 43.10 (2018), pp. 740–745.
- [5] Xiangkun Wu et al. “Safety Issues in Lithium Ion Batteries: Materials and Cell Design”. In: *Frontiers in Energy Research* 7 (2019), p. 96.
- [6] Elise M. Miner, Sarah S. Park, and Mircea Dincă. “High Li⁺ and Mg²⁺ Conductivity in a Cu-Azolate Metal-Organic Framework”. In: *Journal of the American Chemical Society* 141.10 (2019), pp. 4422–4427.
- [7] Mingjie Du et al. “Recent advances in the interface engineering of solid-state Li-ion batteries with artificial buffer layers: challenges, materials, construction, and characterization”. In: *Energy & Environmental Science* 12.6 (2019), pp. 1780–1804.
- [8] Wenjia Zhao et al. “Solid-State Electrolytes for Lithium-Ion Batteries: Fundamentals, Challenges and Perspectives”. In: *Electrochemical Energy Reviews* 2.4 (2019), pp. 574–605.
- [9] Nan Chen et al. “Ionogel Electrolytes for High-Performance Lithium Batteries: A Review”. In: *Advanced Energy Materials* 8.12 (2018), p. 1702675.
- [10] J. M. Tarascon and M. Armand. “Issues and challenges facing rechargeable lithium batteries”. In: *Nature* 414.6861 (2001), pp. 359–367.
- [11] Da Deng. “Li-ion batteries: basics, progress, and challenges”. In: *Energy Science & Engineering* 3.5 (2015), pp. 385–418.
- [12] Yong Lu, Qiu Zhang, and Jun Chen. “Recent progress on lithium-ion batteries with high electrochemical performance”. In: *Science China Chemistry* 62.5 (2019), pp. 533–548.
- [13] Xuebing Han et al. “A review on the key issues of the lithium ion battery degradation among the whole life cycle”. In: *eTransportation* 1.1–2 (2019), p. 100005.
- [14] Wu Xu et al. “Lithium metal anodes for rechargeable batteries”. In: *Energy & Environmental Science* 7.2 (2014), pp. 513–537.

- [15] Kyung Yoon Chung and Kwang-Bum Kim. “Investigations into capacity fading as a result of a Jahn–Teller distortion in 4V LiMn₂O₄ thin film electrodes”. In: *Electrochimica Acta* 49.20 (2004), pp. 3327–3337.
- [16] Hailin Zhang et al. “Recent progress in advanced electrode materials, separators and electrolytes for lithium batteries”. In: *Journal of Materials Chemistry A* 6.42 (2018), pp. 20564–20620.
- [17] Patrick Hossay. *Automotive innovation: The science and engineering behind cutting-edge automotive technology*. First edition. Boca Raton, FL: CRC Press, 2020.
- [18] Sung-Kyun Jung et al. “Understanding the Degradation Mechanisms of LiNi_{0.5}Co_{0.2}Mn_{0.3}O₂ Cathode Material in Lithium Ion Batteries”. In: *Advanced Energy Materials* 4.1 (2014), p. 1300787.
- [19] Hyung-Joo Noh et al. “Comparison of the structural and electrochemical properties of layered Li[Ni_xCo_yMn_z]O₂ (x = 1/3, 0.5, 0.6, 0.7, 0.8 and 0.85) cathode material for lithium-ion batteries”. In: *Journal of Power Sources* 233 (2013), pp. 121–130.
- [20] Jin H. Choi et al. “Thermal Behavior of Ni-Rich Layered Oxide Cathode Materials during Cycling of 20 Ah-Scale Li-Ion Batteries”. In: *Journal of The Electrochemical Society* 165.16 (2018), A3837–A3843.
- [21] Kang Xu. “Electrolytes and interphases in Li-ion batteries and beyond”. In: *Chemical Reviews* 114.23 (2014), pp. 11503–11618.
- [22] R. G. Linford and S. Hackwood. “Physical techniques for the study of solid electrolytes”. In: *Chemical Reviews* 81.4 (1981), pp. 327–364.
- [23] R. C. Agrawal and G. P. Pandey. “Solid polymer electrolytes: materials designing and all-solid-state battery applications: an overview”. In: *Journal of Power Sources* 41.22 (2008), p. 223001.
- [24] Chunwen Sun et al. “Recent advances in all-solid-state rechargeable lithium batteries”. In: *Nano Energy* 33.2012 (2017), pp. 363–386.
- [25] Dechao Zhang et al. “Recent Progress in Organic-Inorganic Composite Solid Electrolytes for All-Solid-State Lithium Batteries”. In: *Chemistry (Weinheim an der Bergstrasse, Germany)* 26.8 (2020), pp. 1720–1736.
- [26] M. M. Elmahdy et al. “Effect of Confinement on Polymer Segmental Motion and Ion Mobility in PEO/Layered Silicate Nanocomposites”. In: *Macromolecules* 39.16 (2006), pp. 5170–5173.
- [27] Zaneta Wojnarowska et al. “Effect of Chain Rigidity on the Decoupling of Ion Motion from Segmental Relaxation in Polymerized Ionic Liquids: Ambient and Elevated Pressure Studies”. In: *Macromolecules* 50.17 (2017), pp. 6710–6721.

- [28] Yonatan Horowitz et al. “Review—Polymer/Ceramic Interface Barriers: The Fundamental Challenge for Advancing Composite Solid Electrolytes for Li-Ion Batteries”. In: *Journal of The Electrochemical Society* 167.16 (2020), p. 160514.
- [29] Yingying Lu et al. “Ionic-liquid-nanoparticle hybrid electrolytes: applications in lithium metal batteries”. In: *Angewandte Chemie (International ed. in English)* 53.2 (2014), pp. 488–492.
- [30] Feng Wu et al. ““Liquid-in-Solid” and “Solid-in-Liquid” Electrolytes with High Rate Capacity and Long Cycling Life for Lithium-Ion Batteries”. In: *Chemistry of Materials* 28.3 (2016), pp. 848–856.
- [31] Surya S. Moganty et al. “Ionic-liquid-tethered nanoparticles: hybrid electrolytes”. In: *Angewandte Chemie (International ed. in English)* 49.48 (2010), pp. 9158–9161.
- [32] Won Seok Chi et al. “Hybrid electrolytes prepared from ionic liquid-grafted alumina for high-efficiency quasi-solid-state dye-sensitized solar cells”. In: *Nanoscale* 5.12 (2013), pp. 5341–5348.
- [33] Nazmul Abedin Khan, Zubair Hasan, and Sung Hwa Jung. “Ionic liquids supported on metal-organic frameworks: remarkable adsorbents for adsorptive desulfurization”. In: *Chemistry (Weinheim an der Bergstrasse, Germany)* 20.2 (2014), pp. 376–380.
- [34] Irene Osada et al. “Ionic-Liquid-Based Polymer Electrolytes for Battery Applications”. In: *Angewandte Chemie (International ed. in English)* 55.2 (2016), pp. 500–513.
- [35] Michael J. Katz et al. “A facile synthesis of UiO-66, UiO-67 and their derivatives”. In: *Chem. Commun.* 49.82 (2013), pp. 9449–9451.
- [36] Rob Ameloot et al. “Ionic conductivity in the metal-organic framework UiO-66 by dehydration and insertion of lithium tert-butoxide”. In: *Chemistry (Weinheim an der Bergstrasse, Germany)* 19.18 (2013), pp. 5533–5536.
- [37] Brian M. Wiers et al. “A solid lithium electrolyte via addition of lithium isopropoxide to a metal-organic framework with open metal sites”. In: *Journal of the American Chemical Society* 133.37 (2011), pp. 14522–14525.
- [38] Mohaddeseh Nasrabadi, Mohammad Ali Ghasemzadeh, and Mohammad Reza Zand Monfared. “The preparation and characterization of UiO-66 metal-organic frameworks for the delivery of the drug ciprofloxacin and an evaluation of their antibacterial activities”. In: *New Journal of Chemistry* 43.40 (2019), pp. 16033–16040.
- [39] Michalina Stawowy et al. “The Impact of Synthesis Method on the Properties and CO₂ Sorption Capacity of UiO-66(Ce)”. In: *Catalysts* 9.4 (2019), p. 309.

- [40] Sheng-Bao Xiao et al. “Stability of Zirconium Metal Organic Frameworks with 9,10- Dicarboxylic Acid Anthracene as Ligand”. In: *Journal of the Korean Ceramic Society* 53.2 (2016), pp. 200–205.
- [41] Yan Cao et al. “UiO-66-NH₂/GO Composite: Synthesis, Characterization and CO₂ Adsorption Performance”. In: *Materials (Basel, Switzerland)* 11.4 (2018).
- [42] Daiane Damasceno Borges et al. “Proton Transport in a Highly Conductive Porous Zirconium-Based Metal-Organic Framework: Molecular Insight”. In: *Angewandte Chemie (International ed. in English)* 55.12 (2016), pp. 3919–3924.
- [43] David L. Bish and Jeffrey E. Post. *Modern powder diffraction*.
- [44] B. D. Cullity. *Elements of x-ray diffraction*. Reading, MA: Addison-Wesley Publishing Company, Inc, 1978.
- [45] Evgenij Barsoukov and James Ross Macdonald, eds. *Impedance spectroscopy: Theory, experiment, and applications*. Hoboken, New Jersey, 2005.
- [46] Vadim F. Lvovich. *Impedance spectroscopy: Applications to electrochemical and dielectric phenomena*. Hoboken, N.J: Wiley, 2012.
- [47] Keith Scott and Eileen Hao Yu. *Microbial Electrochemical and Fuel Cells: Fundamentals and Applications*. Vol. number 88. Woodhead publishing series in energy. Amsterdam et al.: Elsevier Science, 2015.
- [48] Keith Scott and Eileen Hao Yu, eds. *Microbial electrochemical and fuel cells: Fundamentals and applications*. Vol. number 88. Woodhead publishing series in energy. Amsterdam et al.: Woodhead Publishing is an imprint of Elsevier, 2016.
- [49] Mark E. Orazem and Bernard Tribollet. *Electrochemical impedance spectroscopy*. The Electrochemical Society series. 2008.
- [50] W. Hiser, R. W. Penman, and J. T. Reeves. “Preservation of hypoxic pulmonary pressor response in canine pneumococcal pneumonia”. In: *The American review of respiratory disease* 112.6 (1975), pp. 817–822.
- [51] James A. Schwindeman, B. Troy Dover, Robert C. Morrison, Conrad W. Kamienski. “Preparation of lithium alkoxides”. US-5276219-A. 1994.
- [52] Marco Taddei et al. “Aging of the reaction mixture as a tool to modulate the crystallite size of UiO-66 into the low nanometer range”. In: *Chemical communications (Cambridge, England)* 52.38 (2016), pp. 6411–6414.
- [53] Vahid Safarifard and Ali Morsali. “Applications of ultrasound to the synthesis of nanoscale metal–organic coordination polymers”. In: *Coordination Chemistry Reviews* 292 (2015), pp. 1–14.
- [54] Kolja Beltrop et al. “Does Size really Matter? New Insights into the Intercalation Behavior of Anions into a Graphite-Based Positive Electrode for Dual-Ion Batteries”. In: *Electrochimica Acta* 209 (2016), pp. 44–55.

- [55] Hsin-Chieh Huang et al. “Electric double layer capacitors of high volumetric energy based on ionic liquids and hierarchical-pore carbon”. In: *Journal of Materials Chemistry A* 2.36 (2014), pp. 14963–14972.
- [56] Nan Chen et al. “A Li + conductive metal organic framework electrolyte boosts the high-temperature performance of dendrite-free lithium batteries”. In: *Journal of Materials Chemistry A* 7.16 (2019), pp. 9530–9536.
- [57] John T. S. Irvine, Derek C. Sinclair, and Anthony R. West. “Electroceramics: Characterization by Impedance Spectroscopy”. In: *Advanced Materials* 2.3 (1990), pp. 132–138.
- [58] Kazuyuki Fujie and Hiroshi Kitagawa. “Ionic liquid transported into metal–organic frameworks”. In: *Coordination Chemistry Reviews* 307 (2016), pp. 382–390.

A. List of abbreviations

MOF	Metal organic framework
EMIM-FSI	1-Ethyl-3-methylimidazolium bis(fluorosulfonyl)imide
UiO	Universitetet i Oslo
wt%	weight percentage
BET	Brunauer–Emmett–Teller
ATR	Attenuated total reflection
XRD	X-ray powder diffraction
FTIR	Fourier-transform infrared spectroscopy
EV	Electric vehicle
LIBs	Lithium-ion batteries
SSBs	Solid-state batteries
SEI	Solid-electrolyte interphase
ESW	Electrochemical stability window
EC	Ethylene carbonate
PC	Propylene carbonate
DMC	Dimethyl carbonate
DEC	Diethyl carbonate
EMC	Ethyl methyl carbonate
DME	Dimethoxyethane
SEs	Solid electrolytes
ISEs	Inorganic solid electrolytes
SPEs	Solid polymer electrolytes
CSEs	Composite solid electrolytes
LISICON	Lithium superionic conductor
NASICON	Sodium super ion conductor
LIPON	Lithium phosphorus oxynitride
IL	Ionic liquid
BDC	Benzene dicarboxylic unit
EIS	Electrochemical impedance spectroscopy
AC	Alternating Current
DC	Direct current
CPE	Constant phase element
DMF	Dimethylformamide
THF	Tetrahydrofuran
Li3m3p	Lithium 3-methyl-3-pentoxide

B. Appendix

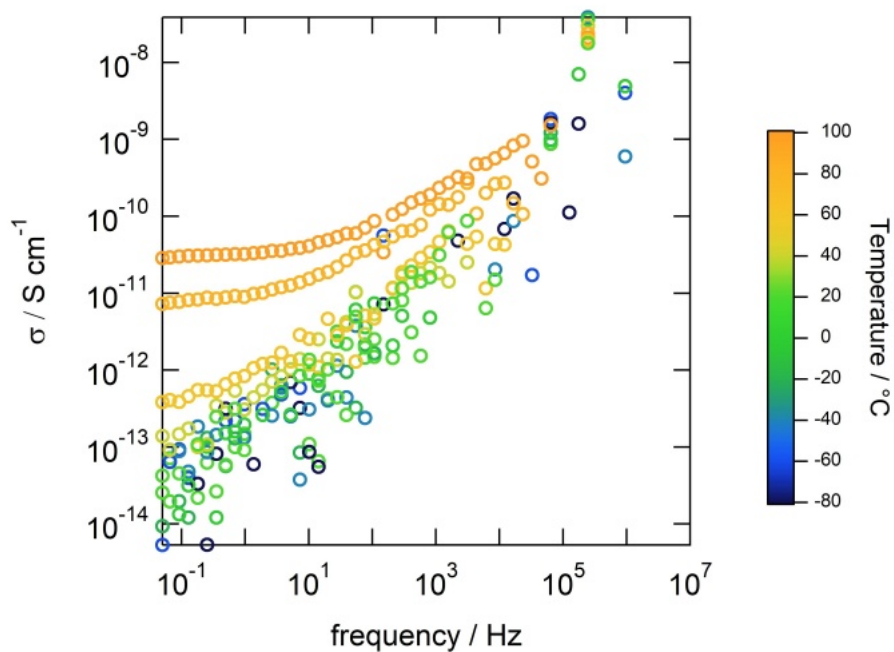


Figure 41: Conductivity isotherms of UiO-66

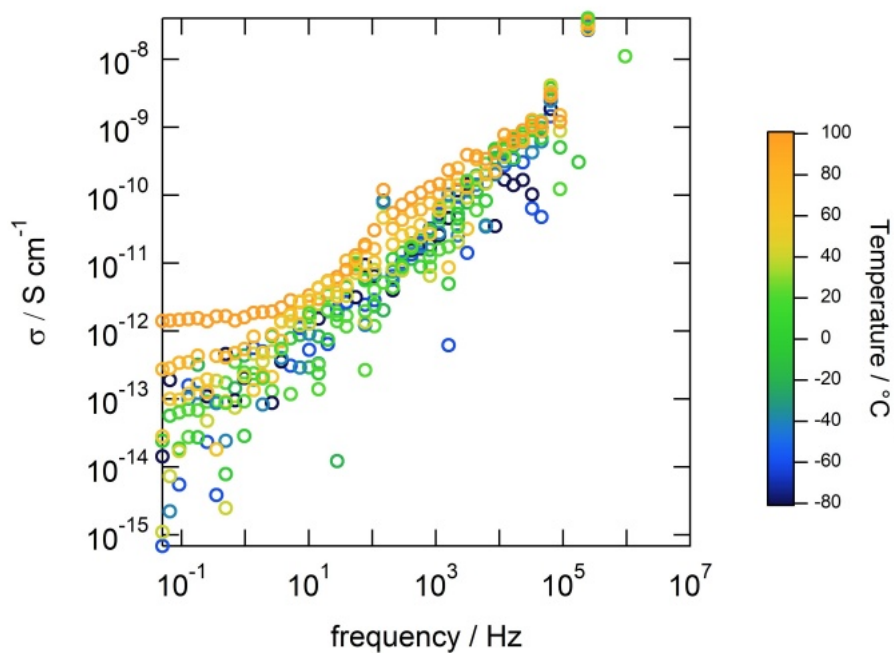


Figure 42: Conductivity isotherms of UiO-66-NH₂

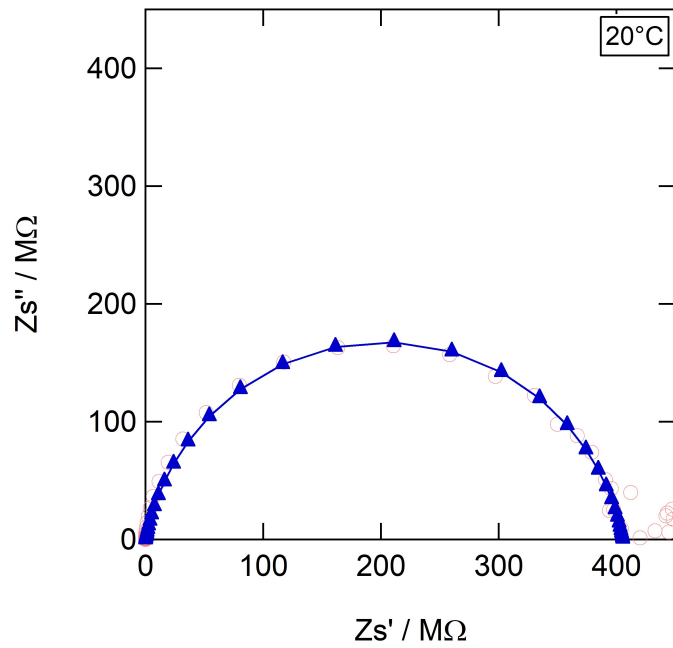


Figure 43: The Nyquist plot of sample **A** and the corresponding fit function. The fit function of the used equivalent circuit is shown in blue and the recorded impedance data in pale red color.

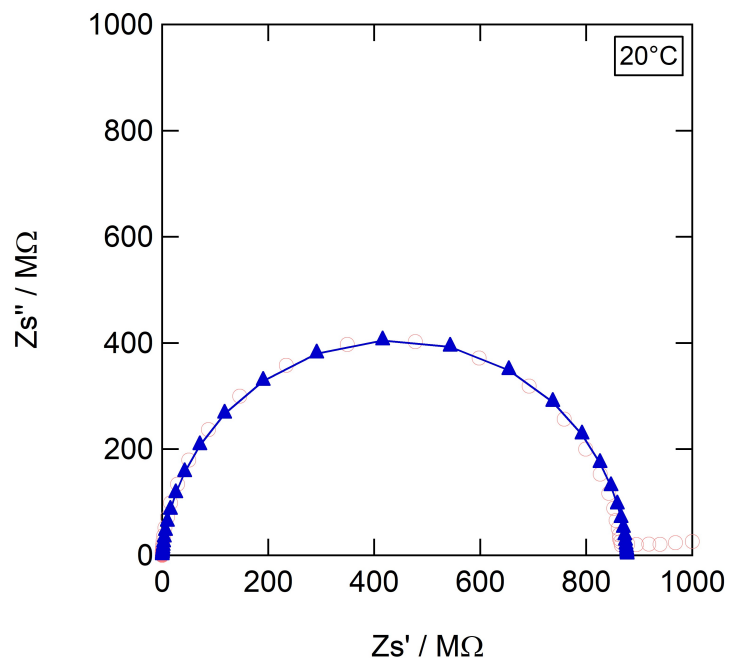


Figure 44: The Nyquist plot of sample **C** and the corresponding fit function.

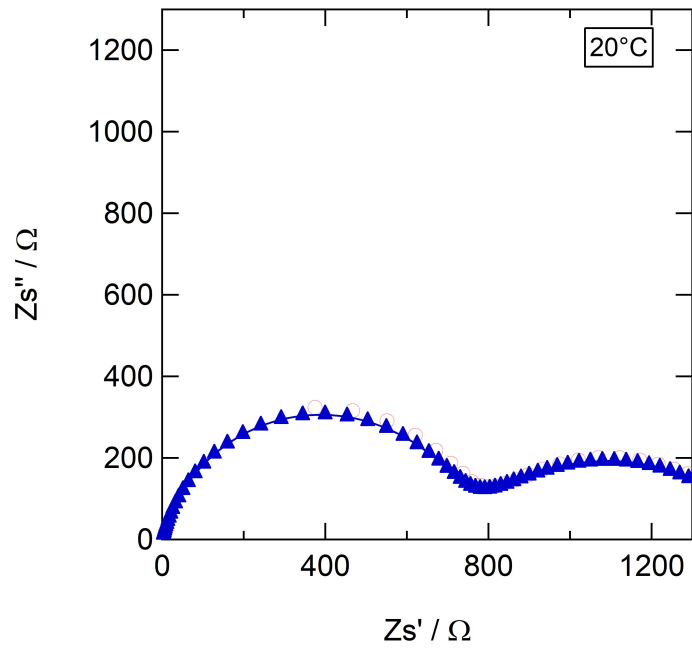


Figure 45: The Nyquist plot of sample **E** and the corresponding fit function.

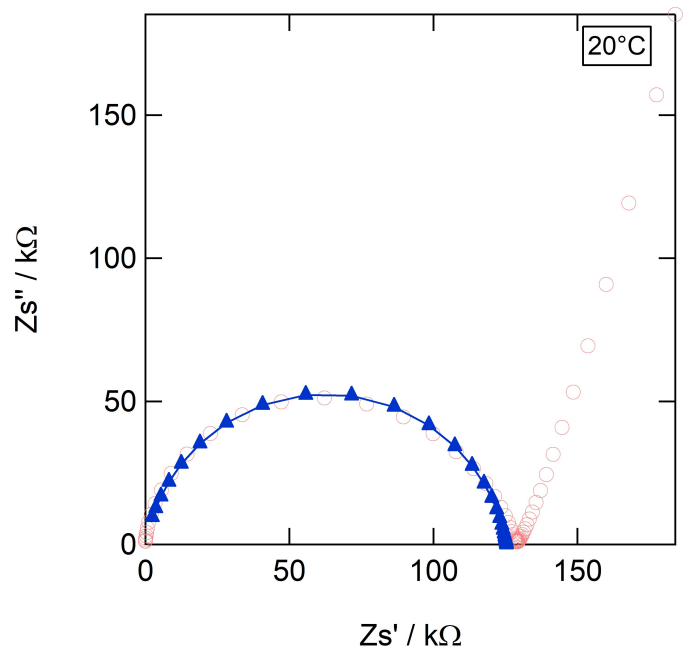


Figure 46: The Nyquist plot of sample **B** and the corresponding fit function.

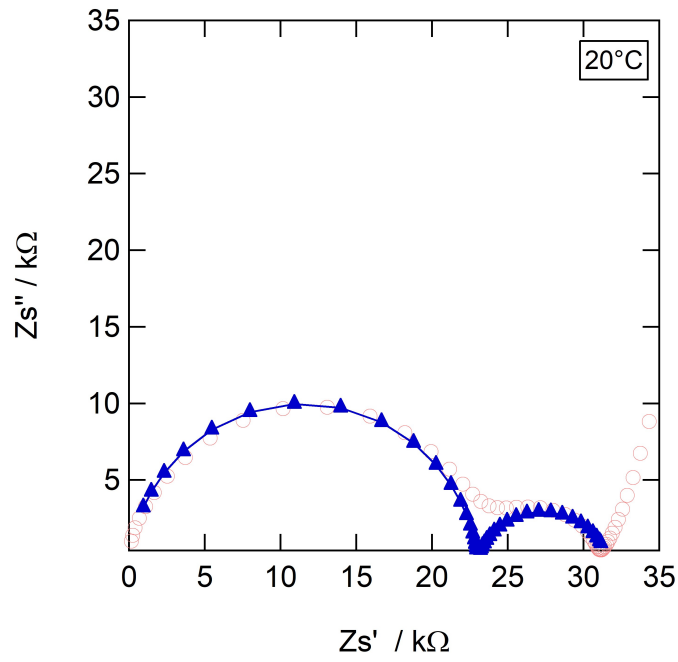


Figure 47: The Nyquist plot of sample **D** and the corresponding fit function.

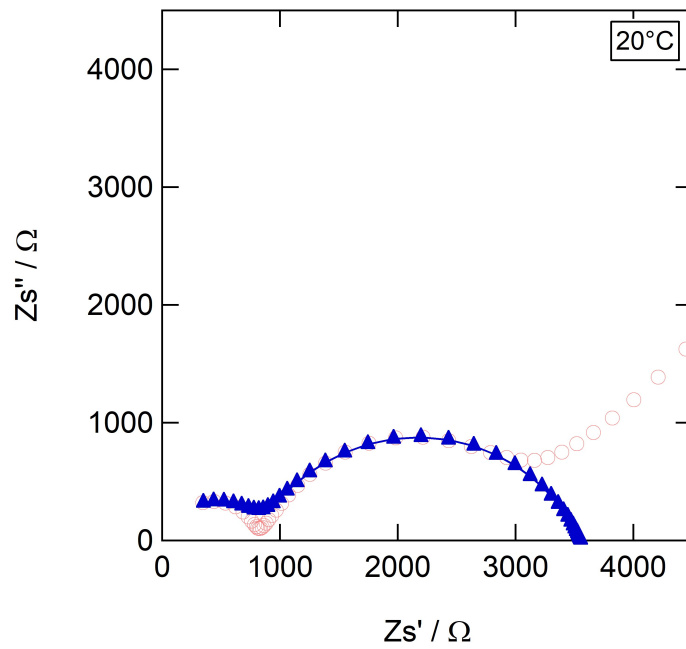


Figure 48: The Nyquist plot of sample **F** and the corresponding fit function.